INFORMATION TO USERS

This manuscript has been reproduced from the microfilm master. UMI films the text directly from the original or copy submitted. Thus, some thesis and dissertation copies are in typewriter face, while others may be from any type of computer printer.

The quality of this reproduction is dependent upon the quality of the copy submitted. Broken or indistinct print, colored or poor quality illustrations and photographs, print bleedthrough, substandard margins, and improper alignment can adversely affect reproduction.

In the unlikely event that the author did not send UMI a complete manuscript and there are missing pages, these will be noted. Also, if unauthorized copyright material had to be removed, a note will indicate the deletion.

Oversize materials (e.g., maps, drawings, charts) are reproduced by sectioning the original, beginning at the upper left-hand corner and continuing from left to right in equal sections with small overlaps.

Photographs included in the original manuscript have been reproduced xerographically in this copy. Higher quality 6" x 9" black and white photographic prints are available for any photographs or illustrations appearing in this copy for an additional charge. Contact UMI directly to order.

Bell & Howell Information and Learning
300 North Zeeb Road, Ann Arbor, MI 48106-1346 USA
800-521-0600

Experimental investigation of direct initiation of quasi-cylindrical detonations

by

Matei Ioan Radulescu

Department of Mechanical Engineering
McGill University
Montréal, Québec, Canada

A thesis submitted to the
Faculty of Graduate Studies and Research
In partial fulfillment of the requirement for the degree of
Master's in Engineering

September 1999

Abstract

Initiation of detonation in the cylindrical geometry is important in validating a general theory of initiation, and has particular significance to the interaction of high velocity projectiles with combustible gas. In the present study, an experimental investigation of the direct initiation of gaseous detonations by a line source of condensed explosives (detonating cord) is presented.

Due to the high velocity of detonation in the condensed explosive cord (6 – 7 km/s), the rapid chemical energy release along its length generates a quasi-cylindrical blast wave in the surrounding combustible mixture. For a sufficiently strong detonating cord, the generated blast wave is observed to decay to a stable Chapman-Jouguet (CJ) conical detonation. Below a certain critical energy, the blast wave decays to low velocities without initiating detonation. In the critical regime of initiation, measurements of the combustion front velocity and direct flow visualization indicate that the blast wave decays to sub-CJ velocities before the onset of detonation. The onset of detonation is associated with discrete explosion centers. This phenomenon is similar to what has been previously observed for spherical initiation, suggesting a universal mechanism of detonation initiation.

The critical shock radius at which the onset of detonation occurs is correlated to the detonation cell size (λ) of the mixture, consistently yielding a radius of 4 to 8λ. Using the invariance of the explosion length R_o in the critical regime of initiation for spherical and cylindrical detonations, it is shown how the critical radii and critical energies scale between the two geometries, clarifying the correct length scales that should be used in the theory of direct initiation of detonation.

Résumé

L'initiation de détonations dans une géometrie cylindrique est importante pour la validation d'une théorie générale d'initiation. De plus, ce problème est intimement relié à l'interaction des projectiles hypersoniques avec un milieu gazeux combustible. Cette thèse présente une étude expérimentale sur l'initiation directe de détonations gazeuses par une charge d'explosif condensé disposé le long d'une ligne (cordon explosif).

Le célérité de détonation dans le cordon explosif étant très grande (6 à 7 km/s), le dégagement rapide d'énergie par le cordon explosif génère une forte onde de choc quasi-cylindrique dans le mélange combustible environnant. Lorsque l'énergie dégagée par le cordon explosif est suffisante, on observe une détonation de Chapman Jouguet (CJ) conique stable. Pour un niveau d'énergie trop bas, l'onde de choc initiale décroît vers une onde acoustique et la détonation n'est pas initiée. Dans le régime critique d'initiation, les mesures de la célerité du front de combustion et les observations photographiques démontrent que l'onde de choc atteint des célérites inférieures à CJ avant l'initiation de la détonation. Dans ce cas, la détonation est initiée par des centres d'explosion isolés. Ce phénomene est similaire à ce qui a été préalablement observé pour l'initiation de détonations sphériques, ce qui suggère un mechanisme universel d'initiation.

Le rayon critique où la détonation est formée a été correlé à la largeur d'une cellule de détonation; on observe un rayon de 4 à 8 λ. En utilisant l'invariance du rayon d'explosion R_o pour l'initiation critique de détonations sphériques et cylindriques, il est démontré comment le rayon critique et l'énergie critique nécessaire pour initier le détonation sont reliés entre les différentes géometries, ce qui clarifie les échelles de longueur caractéristiques appropriées dans la théorie de l'initiation directe des détonations gazeuses.

Acknowledgements

I would like to thank both Andrew Higgins and my thesis supervisor, John Lee, who both taught me everything I know and showed me how it all fits together. Andrew's patience and John Lee's insight were the key factors for my successful completion of this thesis.

I would also like to thank the entire Shock Wave Physics Group at McGill for their continuous support. Igor Fomenko measured the detonating cord blast wave in air, and his contributions to the present work are greatly acknowledged.

Finally, I would like to thank Stephen Murray and Keith Gerrard, whose contributions in the large scale trials carried out at DRES were essential.

Table of Contents

Abstract..... ii

Résumé..... iii

Acknowledgements..... iv

Table of Contents..... v

List of Figures..... vii

List of Tables..... xi

Nomenclature..... xii

Chapter 1 Introduction..... 1

1.1. Background..... 1

1.2. Direct Initiation of Gaseous Detonation..... 2

1.3. Hypersonic Projectile Initiation..... 4

1.4. Outline of the Present Work..... 5

Chapter 2 Detonating Cord in Inert Gas..... 6

2.1. Overview..... 6

2.2. Experimental Details..... 7

2.3. Results and Discussions..... 8

2.4. Summary and Conclusions..... 12

Chapter 3 Detonating Cord in Combustible Gas 14

3.1. Overview..... 14

3.2. General Description of Apparatus and Procedure..... 16

3.3. Mixture Selection and Preparation..... 17

3.4. Diagnostics..... 18

3.5. Reduction of Velocity Measurements..... 18

3.6. Results..... 20

3.6.1. Acetylene-Air Mixtures..... 20

3.6.2. Hydrogen-Air Mixtures..... 22

3.6.3. Ethylene-Oxygen-Nitrogen Mixtures..... 24

3.7. Discussion of Results..... 27

3.8. Comparison with Lee-Vasil'ev Theory of Initiation..... 29

3.9. Concluding Remarks..... 31
Chapter 4 Large Scale Investigation of Detonation Initiation by Detonating Cord..... 33
4.1. Overview..... 33
4.2. Experimental Details and Procedure..... 34
4.3. Diagnostics..... 35
4.4. Results..... 36
4.4.1. The Subcritical Regime..... 36
4.4.2. The Supercritical Regime..... 38
4.4.3. The Critical Regime of Initiation..... 45
4.5. Discussion of Results..... 49
Chapter 5 Geometry Scaling of Direct Initiation..... 52
Chapter 6 Conclusions..... 61
References..... 63
Appendix A The Cellular Structure and CJ Parameters of the Mixtures Investigated..... 69
A1. Cell Sizes..... 69
A1.1. Acetylene-Air Mixtures..... 70
A1.2. Hydrogen-Air Mixtures..... 70
A1.3. Ethylene-Oxygen-Nitrogen Mixtures..... 70
A1.4. Ethylene-Air Mixtures..... 73
A1.5. Methane-Oxygen Mixtures..... 73
A2. CJ Detonation Velocity of the Mixtures Investigated..... 74
Appendix B Raw Results in the Large-Scale Experiments..... 76

List of Figures

Fig. 1.1 Spark schlieren photographs illustrating the critical regime of initiation of spherical detonations in $2C_2H_2$ + 5 O2, P_o = 100 Torr, ignited by a laser spark (From Bach, Knystautas and Lee, 1969)

Fig. 2.1 The blast wave analogy for the detonating cord in air

Fig. 2.2 Diagnostics for measuring time-of-arrival of the blast wave and the detonation in the cord

Fig. 2.3 Experimental *r-t* shock trajectory in air

Fig. 2.4 Normalized experimental and theoretical shock shape in air

Fig. 2.5 Idealized shock interactions at the detonating cord/air interface

Fig. 2.6 Blast wave strength as a function of radial distance

Fig. 3.1 Detonation initiation by detonating cord: *a*) subcritical, *b*) critical, and *c*) supercritical initiation regimes

Fig. 3.2 Experimental apparatus

Fig. 3.3 Experiment schematic

Fig. 3.4 Combustion wave phase velocities

Fig. 3.5 Radial velocity profile for stoichiometric acetylene-air

Fig. 3.6 Axial velocity profile for stoichiometric acetylene-air

Fig. 3.7 Radial velocity profile in hydrogen-air mixtures

Fig. 3.8 Axial velocity profile in hydrogen-air mixtures

Fig. 3.9 Radial velocity profile in ethylene-oxygen-nitrogen mixtures, P_o = 1 bar

Fig. 3.10 Radial velocity profile in ethylene-oxygen-nitrogen mixtures, P_o = 3 bar

Fig. 3.11 Radial velocity profile in ethylene-oxygen-nitrogen mixtures, $P_O = 0.33$ bar

Fig. 3.12 Bow shock wave and combustion front generated by a 9 mm sphere fired into a stoichiometric hydrogen-air mixture ($P_O = 0.55$ atm, $V_{sphere} = 2871$ m/s) (from Struth, Behrens, and Wecken, 1963)

Fig. 4.1 Picture of bag set-up (DRES)

Fig. 4.2 Experiment and instrumentation schematic

Fig. 4.3 Subcritical regime in C_2H_4 – Air (Shot 39, $\phi = 0.67$, $E_S = 520$ kJ/m)

Fig. 4.4 Supercritical regime in C_2H_4 – Air (Shot 52, $\phi = 1.07$, $E_S = 65$ kJ/m)

Fig. 4.5 Supercritical regime in C_2H_4 – Air (Shot 36, $\phi = 0.94$, $E_S = 260$ kJ/m)

Fig. 4.6 Supercritical regime in C_2H_4 – Air (Shot 45, $\phi = 0.76$, $E_S = 520$ kJ/m), *a*) side view, *b*) top view

Fig. 4.7 Effect of finite length of detonating cord (Shot 41, $\phi = 0.98$, $E_S = 260$ kJ/m), frames taken 143 μsec apart

Fig. 4.8 Effect of finite length of detonating cord on the back field (Shot 53, $\phi = 1.08$, $E_S = 65$ kJ/m), frames taken 143 μsec apart

Fig. 4.9 Limit of the supercritical regime in C_2H_4 – Air (Shot 35, $\phi = 0.82$, $E_S = 260$ kJ/m)

Fig. 4.10 Critical regime in C_2H_4 – Air (Shot 47, $\phi = 0.70$, $E_S = 520$ kJ/m), *a*) side view, *b*) top view

Fig. 4.11 Critical regime in C_2H_4 – Air (Shot 44, $\phi = 1.03$, $E_S = 65$ kJ/m), frames 286 μsec apart

Fig. 4.12 Limit of the critical regime in C_2H_4 – Air (Shot 42, $\phi = 0.98$, $E_S = 65$ kJ/m), frames 143 μsec apart

Fig. 4.13 Limit of the critical regime in C_2H_4 – Air (same experiment as Fig. 4.12, head-on view)

Fig. 4.14 Summary of experimental results and comparison with theory

Fig. 4.15 Dependence of critical energy on λ^2 for the cylindrical geometry

Fig. 5.1 Streak photograph of a critically initiated spherical detonation in $2.3C_2H_6 + 3.5O_2 + 3.5N_2$ (taken from Elsworth et al., 1984)

Fig. 5.2 Invariance of explosion length in the cylindrical and spherical geometries

Fig. 5.3 Critical radius scaling between geometries

Fig. 5.4 Comparison between critical energy results of Elsworth (Benedick *et al.*, 1985) in C_2H_4 – Air mixtures in the spherical geometry and theory

Fig. 5.5 Comparison between present results in C_2H_4 – Air and theory

Fig. 5.6 Comparison between critical energies measured by Aminallah *et al.* (1993) in $CH_4 - O_2$ and the present experiments

Fig. A1 Three dimensional structure of a real detonation wave

Fig. A2 Cell width measurements in hydrogen air mixtures at 1 bar initial pressure

Fig. A3 Cell length measurements in stoichiometric ethylene-oxygen with variable nitrogen dilution: effect of initial pressure

Fig. A4 Cell width of stoichiometric ethylene-oxygen with variable nitrogen dilution: effect of nitrogen dilution

Fig. A5 Cell width measurements in ethylene-air for different stoichiometries

Fig. A6 Cell width measurements in methane-oxygen for different stoichiometries

Fig. A7 Chapman-Jouguet detonation velocity and Mach number in ethylene-air

Fig. A8 Chapman-Jouguet detonation velocity and Mach number in methane-oxygen

Fig. B1 Experimental diagnostics for the C_2H_4 – Air large scale experiments

List of Tables

Table 3.1 Summary of results for critical direct initiation by detonating cord of fixed strength

Table 5.1 Critical parameters for direct initiation of planar, cylindrical and spherical detonations

Table A1 Chapman Jouguet detonation velocities for acetylene-air, hydrogen-air and ethylene-oxygen-nitrogen mixtures

Table B1 Summary of the different regimes observed in C_2H_4 – Air mixtures

Table B2 Times-of-arrival of the blast/detonation at the pressure transducers and ionization probes

Table B3 Measures of the detonating cord velocity

Table B4 Blast wave velocity measured from the pressure transducers TOA's along the pad floor (in km/s)

Table B5 Velocity measurements between the detonating cord and the pressure transducers on the pad floor

Nomenclature

E_O	re-initiation energy in a detonation cell
E_S	source energy
E_S*	critical initiation energy
j	geometric index (j = 1, 2, 3 for planar, cylindrical, and spherical)
k	arbitrary coefficient in phenomenological initiation models
l	cell length
M_{CJ}	CJ Mach number in the gas
M_S	shock Mach number
M_S*	critical shock strength
n	proportionality coefficient in the elementary cell model
P_{CJ}	CJ pressure in the high explosive
P_O	initial pressure
r	radial coordinate
R_{cord}	detonating cord radius
R_O	explosion length
R_S	shock radius
R_S*	critical radius
t	time
T_O	initial temperature
V	normal shock velocity
V_{CJ}	CJ detonation velocity in the gas
V_{DC}	detonation velocity in the detonating cord
V_R	shock phase velocity in the radial direction
V_X	shock phase velocity in the axial direction
x	axial coordinate

Acronyms

CJ	Chapman Jouguet
DDT	Deflagration to Detonation Transition

HE	High Explosive
TOA	Time of Arrival
VOD	Velocity of Detonation

Greek

α	blast wave constant
β	nitrogen/oxygen composition ratio
δ_P	angle of the interface between the high explosive products and the shocked gas
δ_S	angle of the oblique shock
ϕ	fuel-oxidizer equivalence ratio
γ	ratio of specific heats
γ_{prod}	polytropic index of the high explosive products
λ	detonation cell width
θ	conical detonation half angle
ρ_O	initial density
τ	chemical induction time

Chapter 1 Introduction

1.1 Background

The sensitivity of a combustible mixture to detonation is of importance with respect to explosion hazards. Generally, there are two ways detonation can form. A combustible mixture can be ignited by a low energy source and burn as a slow flame. Then, under appropriate conditions, it can accelerate and undergo a transition to detonation. This phenomenon is referred to as *deflagration to detonation transition* (DDT). Turbulence and interactions between pressure waves and the flame are the principal flame acceleration mechanisms that generate the critical state for the onset of detonation. In general, the ignition source plays little role in the DDT process. Comprehensive reviews of DDT phenomena have been published by Lee and Moen (1980), Shepherd and Lee (1992), and Sichel (1992).

Alternatively, detonation can also be initiated "instantaneously" when a sufficiently powerful igniter is used. This mode is called *direct initiation*, since detonation is formed directly, without a pre-detonation deflagration regime. It is also sometimes referred to as blast initiation, to emphasize the strong blast wave generated by the igniter. With a strong igniter, two possible outcomes have been observed experimentally. For sufficiently large amounts of energy deposition, the blast wave decays asymptotically to the Chapman Jouguet (CJ) detonation velocity of the mixture. In this case, a self-supported detonation has been successfully initiated in the gas. Below a certain minimum source energy, the reaction zone de-couples from the strong blast, becoming a low speed flame. In this case the source has failed to initiate a detonation. Hence, the energy release of the source must be beyond a certain threshold level, known as the *critical energy*, to successfully initiate detonation.

The initiation phenomenon is quite complex when the energy of the source is close to the critical energy for initiation. At early times, the blast and reaction front are coupled as in an overdriven detonation. As the blast expands and decays, de-coupling occurs and the reaction front initially recedes from the shock. As the chemical energy begins to influence the blast motion, the blast no longer decays,

Fig. 1.1 Spark schlieren photographs illustrating the critical regime of initiation of spherical detonations in $2C_2H_2 + 5O_2$, $P_o = 100$ Torr, ignited by a laser spark (from Bach, Knystautas and Lee, 1969)

and the shock-flame complex is seen to propagate at a quasi-steady velocity near the auto-ignition limit of the mixture. This regime is termed the "quasi-steady regime". A quasi-steady regime is also observed in deflagration to detonation transition (DDT) prior to the onset of detonation (Chue, 1993). The quasi-steady regime abruptly ends with the formation of micro-explosions behind the leading shock. These localized explosions immediately form "detonation bubbles" which propagate in the shocked layer of unburned gas behind the blast wave and coalesce to eventually form a stable CJ detonation. Classic schlieren photographs of this process can be found in Bach *et al.* (1969), as shown in Fig. 1.1.

1.2 Direct Initiation of Gaseous Detonation

The first theoretical model for direct initiation in the spherical geometry was proposed by Zeldovich, Kogarko and Simonov (1956). Zeldovich *et al.* postulated that the required source energy for successful initiation of detonation should satisfy the conditions that: a) the blast wave generated should be of sufficient strength (with pressure $P > P_{CJ}$) for triggering the chemical reactions, and b) the blast wave should be of adequate duration (larger than the chemical induction time), to permit chemical reactions to go to completion. Zeldovich *et al.* then arrived at the cubic dependence of the critical energy on the chemical induction time of the mixture ($E_s^* \sim \tau^3$). Although Zeldovich's criterion is qualitative, it led to the correct

qualitative dependence of the initiation energy on the reaction kinetics of the mixture.

Since Zeldovich's pioneering study, numerous theoretical models were developed to yield a predictive theory. Excellent review of these models can be found in the works of Lee (1977), Lee (1984), Benedick *et al.* (1985), Vasil'ev *et al.* (1988), and Lee and Higgins (1999). However, a complete model able to predict critical energy from the thermo-chemical data of the mixture alone is still lacking. All the existing models are phenomenological in nature, in the sense that they require some input parameters obtained from experiment. These models relate the critical energy for initiation to some characteristic length scale of detonation obtained experimentally (e.g. the detonation cell size λ). The cell size can be readily measured experimentally using the "smoke foil" technique (Strehlow, 1969). A large database for the detonation cell size has recently been compiled by Kaneshige and Shepherd (1997) and is available on the World Wide Web.

The existing phenomenological models for initiation of gaseous detonation have been extensively studied and compared with experiments for spherical detonations in a wide range of fuel-air mixtures. Benedick *et al.* (1985), for example, present experimental measurements of the critical mass of condensed explosive required to initiate spherical detonations in various hydrocarbon-air mixtures. A comparison of the experimental results with different theories was given by Benedick *et al.* (1985) and by Vasil'ev (1997). However, for the initiation of planar and cylindrical detonations, no extensive comparison with experiment has been made, due to the lack of experimental data.

The point source required for direct initiation of spherical detonations appears to be the easiest geometry to realize experimentally. However, for cylindrical and planar detonations, line and planar sources present considerable challenges in experimental implementation. The present study will focus mainly on problems associated with cylindrical detonations. Prior experiments with the initiation of cylindrical detonations have used either spark gaps (Matsui and Lee, 1977) or exploding wires (Aminallah *et al.* 1993, Vasil'ev, 1983), where the length of the line source as well as the amount of energy that can be deposited are quite limited. These sources also invoke a number of non-idealities. The limited length

of the spark gap or exploding wire necessitates the use of a narrow chamber, and hence introduce significant interaction with the chamber walls. Non-idealities due to confinement effects are also present in investigations utilizing condensed explosive charges to initiate cylindrical detonations in a narrow chamber (Vasil'ev and Grigoriev, 1980) or a sectored chamber (Fry and Nicholls, 1969, Nicholls *et al.*, 1978).

1.3 Hypersonic Projectile Initiation

A considerable amount of interest has been directed in recent years toward the flight of high velocity projectiles in a gaseous detonable media. Much of this interest results from propulsion applications using a stabilized detonation wave, e.g. the ram accelerator (Hertzberg *et al.*, 1988, Smeets, 1995) and the oblique detonation engine (Pratt *et al.*, 1991). A theory to predict the requirement for a high-velocity projectile to initiate detonation in a combustible gas was first developed by Lee (Lee, 1965), who proposed the use of the hypersonic blast wave analogy for cylindrical detonations. The theory was developed further by Lee (1997) and Vasil'ev (1994). The Lee and Vasil'ev theory invokes the hypersonic blast wave analogy and states that the work done by the drag of the projectile per unit length should be equal to the critical energy per unit length for the initiation of a cylindrical detonation.

Experimentally, detonation initiation by high-velocity projectile was studied by Ruegg and Dorsey (1962), Behrens, Struth and Wecken (1965), Lehr (1971), McVey and Toong (1971), and more recently by Higgins and Bruckner (1996), Kaneshige and Shepherd (1996), and Endo *et al.* (1997). However, only Higgins and Bruckner have determined the critical conditions for direct initiation, permitting a direct comparison with the Lee-Vasil'ev theory. The limited experimental data of Higgins show good agreement with the theory of Lee and Vasil'ev. The gas-gun-launched projectiles, however, are limited to rather low velocities of the order of the CJ detonation speed. At these low velocities, the validity of the hypersonic blast wave analogy, on which the Lee and Vasil'ev model is based, becomes questionable. Furthermore, limitations on the size of projectiles that can be used permitted only a narrow range of mixture compositions that can be studied. Thus,

the theory of Lee and Vasil'ev has yet to be compared with experiments over a wide range of conditions in the regime in which it was formulated: when the velocity of the energy deposition is much more rapid than the sound velocity in the combustible gas.

1.4 Outline of the Present Work

In the present study, a line source consisting of condensed explosive (detonating cord) is used for initiation. The expansion of the condensed explosive detonation products produces a traveling strong bow shock in the medium, analogous to that of a hypervelocity projectile. The high detonation speed in the condensed explosive cord (6-8 km/sec) is significantly larger than the typical velocity of gun-launched projectiles (~1-3 km/sec). The detonating cord is thus closer to the ideal limit of the hypersonic blast wave analogy, making it an excellent quasi-instantaneous line energy source. The detonating cord is also a source that can be accurately quantified in terms of the amount and rate of energy deposition. The length of detonating cord can be made arbitrarily long, allowing a long chamber to be used, thus eliminating interaction with the end walls.

The present thesis is composed of five chapters. The dynamics of the blast wave generated by the detonating cord in air are studied in Chapter 2. In Chapter 3, the first set of laboratory-scale experiments on the direct initiation of combustible mixtures are presented. The experimental results are then compared with the Lee-Vasil'ev theory. In Chapter 4, a second series of large scale experiments are reported, for which the range of mixture compositions studied are extended and stronger detonating cords are used. Flow visualization is also used in the large-scale experiments to permit photographic observations of the different regimes of initiation. In Chapter 5, discussions of the results found and development of scaling laws that link the cylindrical and the spherical geometry are presented, followed by concluding remarks.

Chapter 2 Detonating Cord in Inert Gas

2.1 Overview

It is of interest to first study the characteristics of the blast wave generated by the detonating cord in an inert medium (air). The bow shock resulting from the detonation wave propagating in a high explosive detonating cord in air is analogous to the bow shock around a hypersonic projectile. In both cases, energy is rapidly deposited along a line. For the projectile, the energy deposition is effected by the projectile, as work done by the drag of the projectile in the surrounding gas. For the detonating cord, the energy is liberated by the detonation of the high explosive inside the cord. The bow shock is driven by the expansion of the high pressure detonation products. Since the velocity of the detonation wave in the explosive cord is a constant, the bow shock is "translated" along the cord's axis at the detonation velocity of the high explosive. An explanatory sketch of the resulting flowfield is shown in Fig. 2.1.

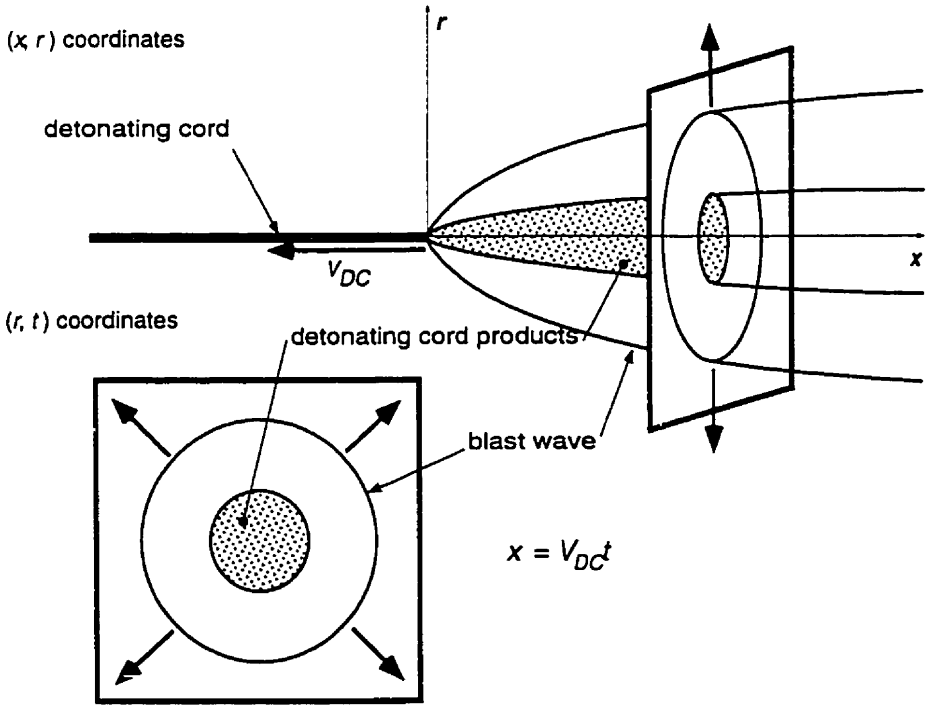

Fig. 2.1 The blast wave analogy for the detonating cord in air

2.2 Experimental Details

The detonating cord used in this study consists of a high explosive PETN core with a plastic PVC cover of 3.1 mm diameter. The explosive content of the cord is 4.9 g/m. The initial density of the PETN powder in the cord is approximately 1.2 g/cm^3. Experiments were performed with one and three cords braided together, yielding equivalent energies[1] of 30 and 90 kJ/m. To determine the shock shape, the detonating cord was placed vertically in the center of a blast chamber and initiated at the top end with a blasting cap. The bow shock shape was determined by the time of arrival of the shock front at fixed radial positions. A total of eight probes were placed along a supporting rod at measured radial distances from the cord (c.f. Fig. 2.2). The probe assembly was placed perpendicular to the charge axis for the blast wave measurements or along the charge axis for the measurements of detonation velocity in the cord. The contact gauge probes consisted of thin plastic strips (0.1 mm thickness) with a centered 7 mm diameter hole "sandwiched" between two conducting brass strips (0.04 mm thick). Upon arrival, the high pressure across the bow shock closes the electric contact between the two brass foil electrodes. This contact is used to generate an electrical pulse by capacitor discharge, which is send to the recording equipment. The time of arrival of the shock at the location of each probe is thus detected. The response time of such a gauge is estimated to 1-10 μsec over the shock range of interest.

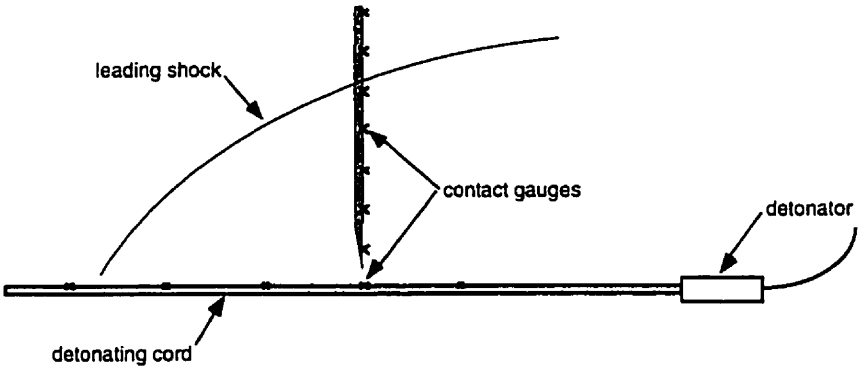

Fig. 2.2 Diagnostics for measuring time-of-arrival of the blast wave and the detonation in the cord

[1] The heat of detonation of PETN is 6.322 kJ/g (taken from Dobratz and Crawford (1985))

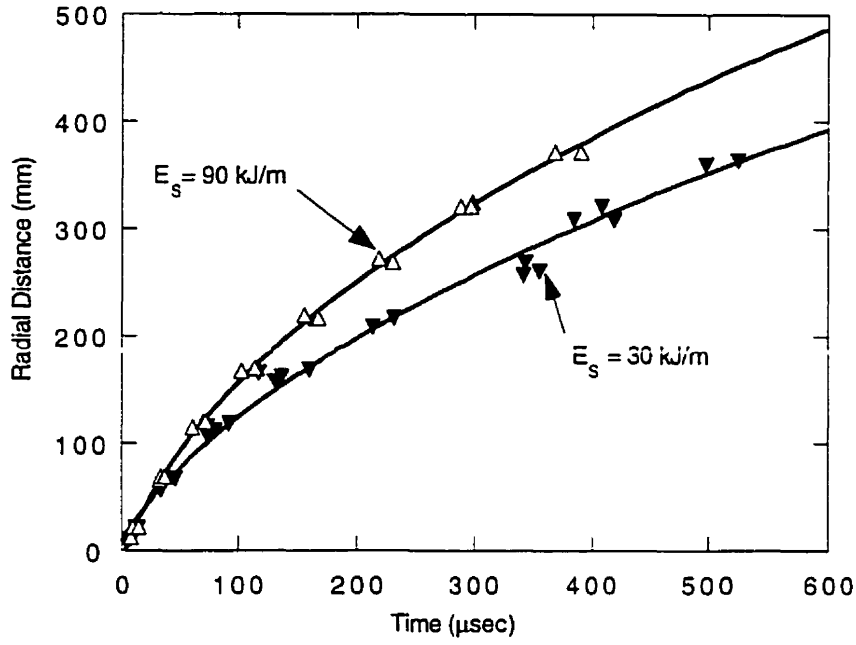

Fig. 2.3 Experimental *r-t* shock trajectory in air

2.3 Results and Discussions

The measured results of the time of arrival of the bow shock wave in the radial direction are shown in Fig. 2.3 for source energies of 30 and 90 kJ/m. The resulting *r-t* shock trajectory describes the dynamics of the expanding shock wave in the radial direction. The slope of these lines represents the velocity of the diverging shock wave. From the slope of the trajectories, it can be seen that the radial wave started out with a high velocity and decelerated as it expanded radially. Consistent with energetic considerations, the bow shock resulting from the weaker cord decayed more rapidly.

The detonation velocity V_{DC} of the high explosive cord determined experimentally is found to be 6.35 ± 0.05 km/sec. The bow shock shape in the spatial *r-x* coordinates can be constructed from the *r-t* radial shock trajectory by using the simple transformation $x = V_{DC}t$ relating the axial coordinate to the time variable of the shock trajectory (see Fig. 2.1). The resulting bow shock shapes are shown in Fig. 2.4 for the two different source energies, 30 and 90 kJ/m. The radial and axial coordinates x and r are normalized by the characteristic explosion length R_0 (i.e. for a cylindrical blast, $R_0 \equiv (E_s/P_0)^{1/2}$). It can be seen that the two

sets of data points collapse onto a same curve, as predicted by energy scaling from blast wave theory. The fact that the results scale with the cylindrical explosion length suggests that the flow is indeed quasi-cylindrical and reflects the cylindrical geometry.

The approximation of a quasi-cylindrical flowfield is in accord with the hypersonic small disturbance theory (Chernyi, 1961, Hayes, 1966). The theory is applicable to slender (low aspect ratio) hypersonic projectiles. Under these conditions, the motion of the bow shock around the projectile can be analyzed conceptually as a series of infinitesimally thin slices, where the blast expands radially with negligible axial dependence, or in other words, a quasi-cylindrical flow. The bow shock dynamics around the detonating cord clearly meet these conditions. The velocity of propagation in the axial direction is hypersonic ($M_{DC} \approx 20$). The bow shock angle, as deduced from the measured shock r-x trajectory, is indeed slender beyond the region in the immediate vicinity of the cord. Based on this quasi-cylindrical approximation, the radial shock trajectory, and consequently the shock shape, can be modeled by cylindrical blast wave theory.

As a first approximation, the theoretical shock shape can be obtained from the classic similarity solution of Lin (1954) for a strong cylindrically expanding blast wave

$$R_S = \left(\frac{E_S}{\alpha_2 \rho_O}\right)^{\frac{1}{4}} t^{\frac{1}{2}} = \left(\frac{E_S}{\alpha_2 \rho_O}\right)^{\frac{1}{4}} \left(\frac{x}{V_{DC}}\right)^{\frac{1}{2}} \qquad 2.1$$

where E_S is the energy per unit length of the source, and α_2 is a blast parameter, which is a weak function of the specific heat ratio γ (for air, $\gamma = 1.4$, $\alpha_2 = 0.986$). However, the strong blast solution is only accurate in the strong shock regime, i.e. for $M_S > 3$. For the moderate shock strength regime, the blast decay is given by the perturbation solution of Sakurai (1953, 1954) and Bach and Lee (1969). In Fig. 2.4, the theoretical shock shape obtained from the perturbation solution and the similarity solution for cylindrical blast waves are compared to the experimentally determined shock shape. Firstly, it can be seen that the shock trajectories obtained via the similarity solution for strong shock and the perturbation solution for finite strength shock do not show any observable differences over the range of shock strengths in the experiment. For shock radii greater than ~$0.2R_O$, or ~$70R_{cord}$, good

agreement is found between the experimental points and the theoretical blast wave solutions. The agreement between the theoretical solution and the experimental results confirm the validity of blast wave theory.

In the vicinity of the cord, the characteristic length scale R_{cord} (cord radius) influences the blast dynamics. For $0.02 \leq R_S/R_O \leq 0.2$, or equivalently $7 \leq R_S/R_{cord} \leq 70$, the blast dynamics are no longer governed by the line-blast theory (Fig. 2.4). A power law fit of the experimental data points in this range suggests that the shock has a nearly constant angle $\delta_S \approx 13°$, and corresponds to a velocity of about 1.5 km/sec, or a shock strength of $M_S \approx 4.5$. This suggests that the near field shock propagation is due to a piston effect of the expanding high explosive detonation products. Only when $R_S >> R_{cord}$, when the relevant length scale becomes the explosion length R_O, does the blast wave approach the dynamics of line-blast decay. Similar effects of the asymptotic approach to ideal blast theory has been observed for spherical blast waves resulting from finite radius, high explosive charges (Brode, 1959, Wecken, 1951).

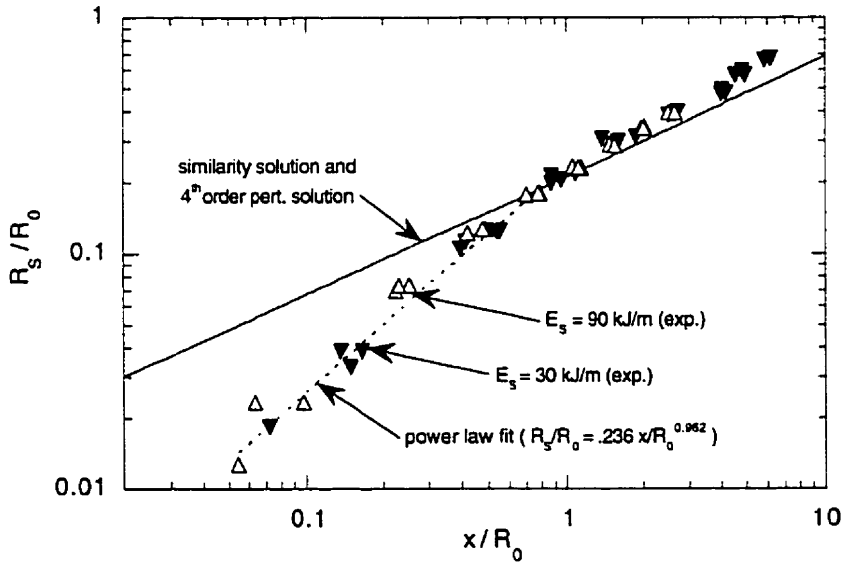

Fig. 2.4 Normalized experimental and theoretical shock shape in air

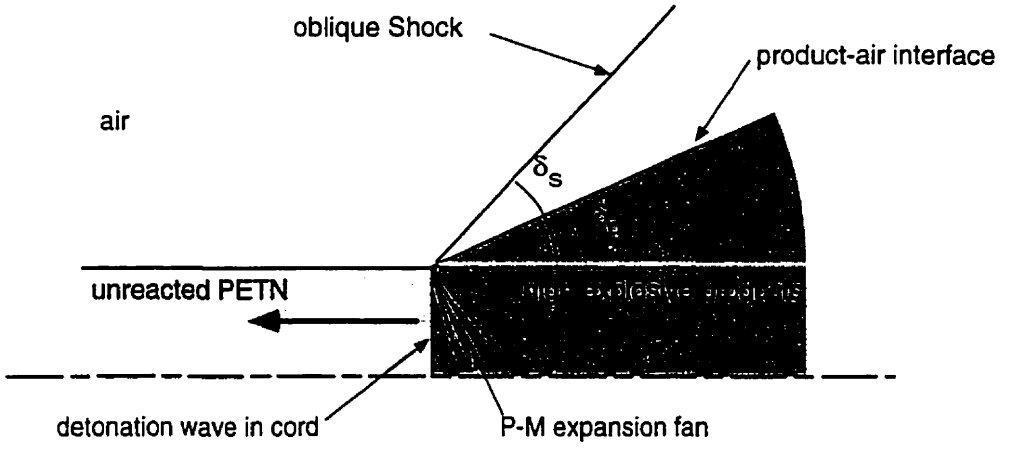

Fig. 2.5 Idealized shock interactions at the detonating cord/air interface

In the immediate vicinity of the detonating cord, the shock is very strong. Even though the resolution of these experimental measurements cannot capture this behavior at distances very close to the source, the initial shock inclination and initial wave strength can be estimated analytically, following the analysis of Sommers and Morrison (1962). The initial shock angle δ_S is estimated by considering a simple two-dimensional model of the shock interaction between the high explosive detonation products and the surrounding air (cf. Fig. 2.5). The wave pattern is modeled by an infinitely thin planar detonation wave in the cord, an oblique shock in air and a Prandlt-Meyer expansion fan in the explosive products, starting at the CJ plane. The CJ states of the PETN explosive products are obtained from the standard equilibrium code CHEETAH (Fried, 1996) (i.e. P_{CJ} = 12.3 GPa, γ_{prod} = 2.9, $V_{DC} = V_{CJ}$ = 6.35 km/sec). The flow pattern is solved by matching pressures and turning angles at the interface between the shocked air and the expanded detonation products. The computed initial deflection angle δ_p and shock angle δ_S are respectively found as 34° and 43°. Using the initial shock angle, the radial velocity of the bow shock is readily determined as $V_R \approx V_{DC} \tan \delta_S \approx 6.3$ km/sec, or $M_S \approx 19$. In this region, the hypersonic small disturbance theory is no longer valid, since the shock angle is not small. This

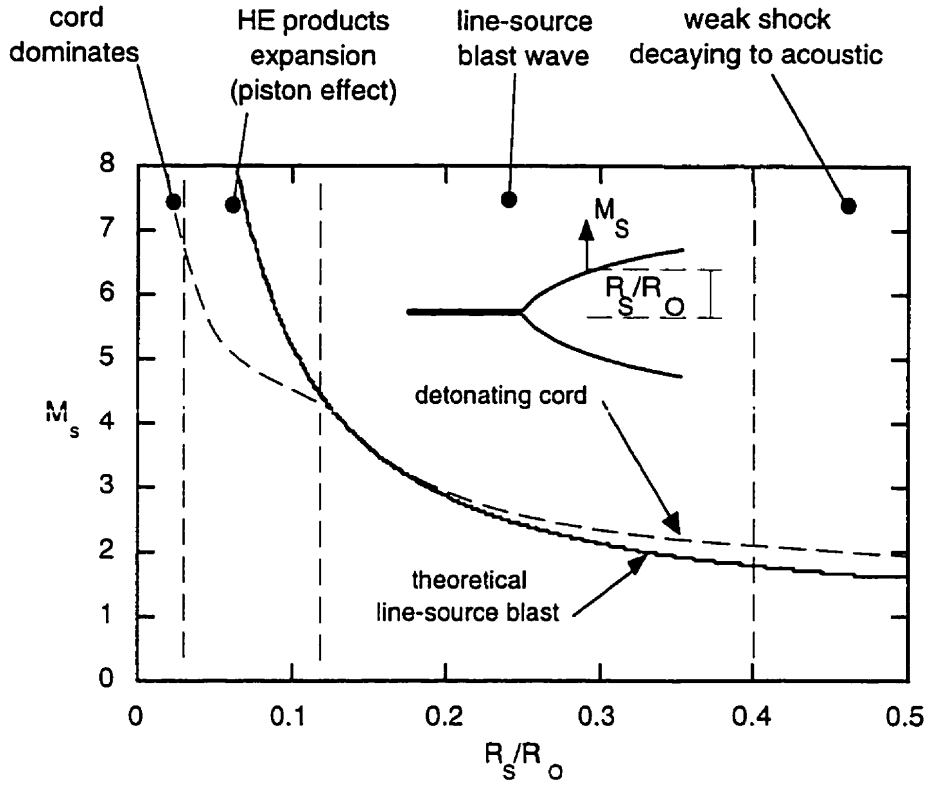

Fig. 2.6 Blast wave strength as a function of radial distance

simple analysis only serves as an upper limit estimate of the velocity of the initial shock in very close proximity to the cord. At larger radii, the shock motion will still be governed by the two-dimensional axi-symmetric effects of the expansion of the products. Only when $R_S >> R_{cord}$ and the near field effects become negligible can the flow be modeled by classical cylindrical line blast theory.

2.4 Summary and Conclusions

The blast characteristics and the different ranges of validity are summarized in Fig. 2.6, where the shock strength M_S is plotted versus increasing normalized radial distance R_S/R_O. The solid line in Fig. 2.6 corresponds to the theoretical perturbation solution for a cylindrical blast wave, and the broken line indicates the trends obtained experimentally. The important features of the bow shock dynamics deduced from experimental and theoretical considerations are summarized below.

- The immediate vicinity of the cord, for $R_S \approx R_{cord}$, is governed by two-dimensional axi-symmetric effects due to the rapid expansion of the high explosive products. The shock wave is initially highly overdriven ($M_S \approx 13$) and decays rapidly afterward.
- In the region $7R_{cord} \leq R_S \leq 70R_{cord}$, the bow shock motion is governed by the quasi-cylindrical piston-like motion of the expanding detonation products.
- In the far field, for $R_S >> R_{cord}$, piston effects become negligible and the flow can be modeled by the ideal cylindrical line-blast theory until the wave decays to acoustic velocities.
- The quasi-cylindrical assumption is valid over the entire range of blast travel, but breaks down in the near vicinity of the cord.

Chapter 3 Detonating Cord in Combustible Gas

3.1 Overview

The blast wave from a detonating cord is generated by the expansion of the high explosive products of the cord. Away from the immediate vicinity of the cord, the dynamics of the blast wave are governed solely by the amount of energy deposition from the detonating cord (c.f. Chapter 2). When the blast wave propagates in a combustible mixture, chemical reactions are initiated by this blast wave. After the initial overdriven region near the cord, if the amount of energy deposition is below a critical value, the shock and combustion front will decouple. This is referred to as the subcritical regime of direct initiation. In this case, the shock decays to sonic velocities, similar to the non-reacting case (c.f. Chapter 2). An explanatory sketch is given in Fig. 3.1a.

If the energy liberated by the detonating cord is above a certain critical value, the chemical reactions can remain coupled to the leading shock (supercritical regime). The blast wave now decays to the Chapman Jouguet detonation velocity of the mixture (~ 2 km/s) and then propagates steadily at this velocity. The initiation events are synchronized with the travelling detonation wave along the cord. Thus, an oblique conical detonation front is formed in the gaseous mixture (Fig. 3.1b), with half angle $\theta = \sin^{-1}(V_{CJ}/V_{DC})$, which translates along the length of the cord with velocity V_{DC}.

The phenomenon is more complex when the energy liberated by the detonating cord is close to the critical initiation energy. The results previously observed for the initiation of spherical detonations in the critical regime indicate that the blast wave does not decay monotonically to a CJ detonation wave. Instead, after the blast wave decays to some sub-CJ velocity, the final onset of detonation is usually associated with the abrupt appearance of localized explosion centers within the shocked gas layer. These explosion centers then grow to encompass the shocked gas, finally merging to produce a detonation. A sketch of

the flowfield in the critical regime of initiation by detonating cord is shown in Fig. 3.1c.

In the present chapter, these different initiation regimes are investigated experimentally by measuring the velocity profiles of the combustion front. For a given strength of cord, "go" or "no-go" conditions for initiation of detonation are determined by changing the sensitivity of the mixture.

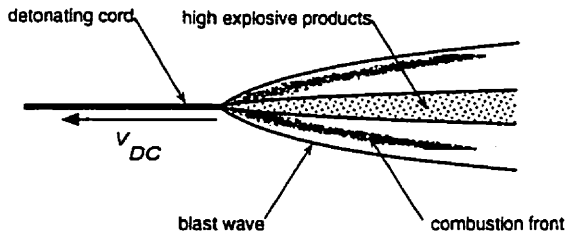

a. $E_{cord} << E_{critical}$

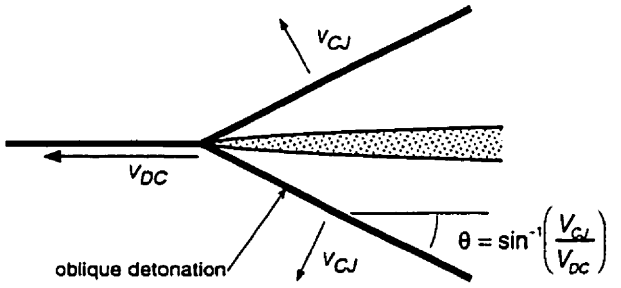

b. $E_{cord} >> E_{critical}$

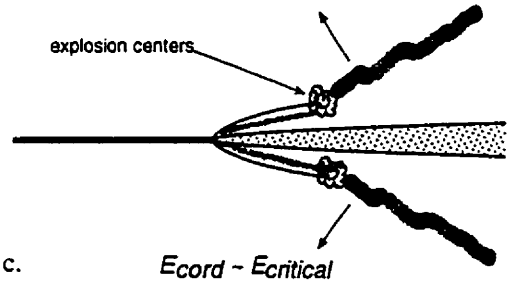

c. $E_{cord} \sim E_{critical}$

Fig. 3.1 Detonation initiation by detonating cord: a) subcritical, b) supercritical, and c) critical initiation regimes

3.2 General Description of Apparatus and Procedure

The experiments were performed in a steel cylindrical blast chamber, 77.5 cm long and 48.5 cm in diameter. The blast chamber is shown in Fig. 3.2. The chamber contained the combustible fuel-oxidizer mixture of interest. The high explosive detonating cord was installed along the central axis of the cylindrical blast chamber. The strength of the detonating cord used in all the experiments was 30 kJ/m (c.f. Chapter 2). The detonating cord was initiated by a Number 8 electric detonator. An elastic band attached to one end of the cord ensured that it remained taut. The chamber was sealed and positioned vertically before firing, so the cord would not sag due to gravity. A schematic of the experimental set-up is shown in Fig. 3.3.

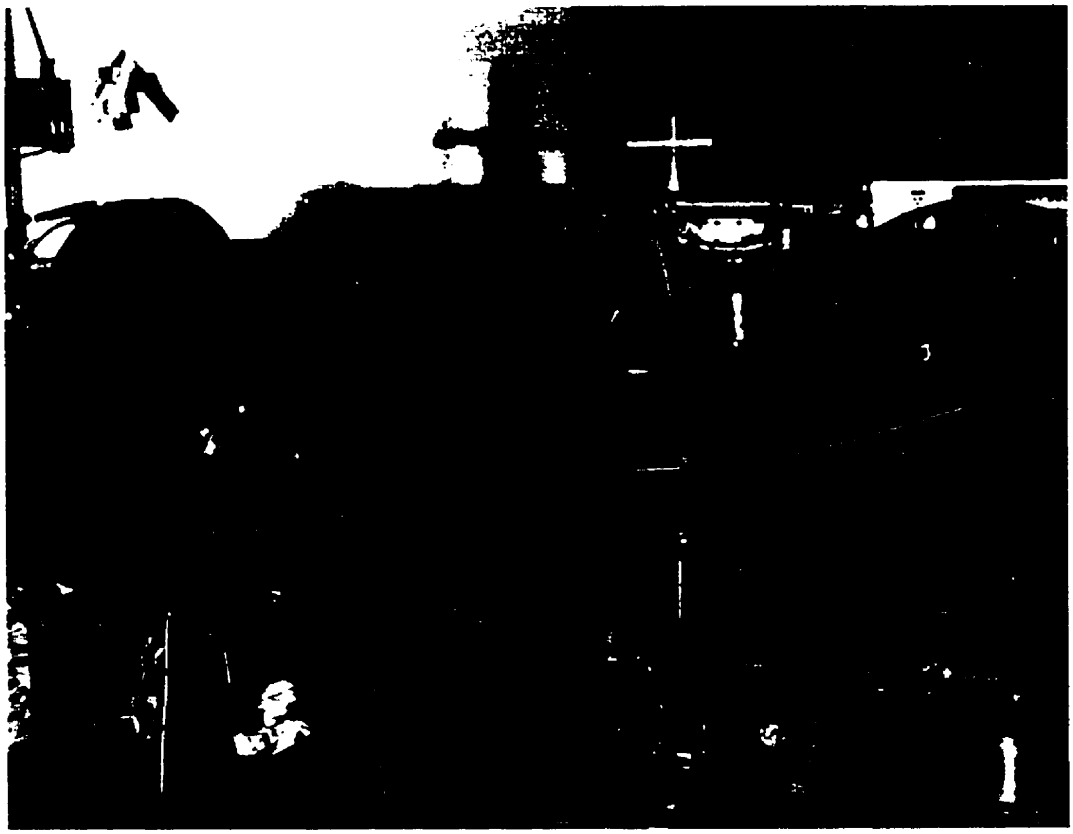

Fig. 3.2 Experimental apparatus

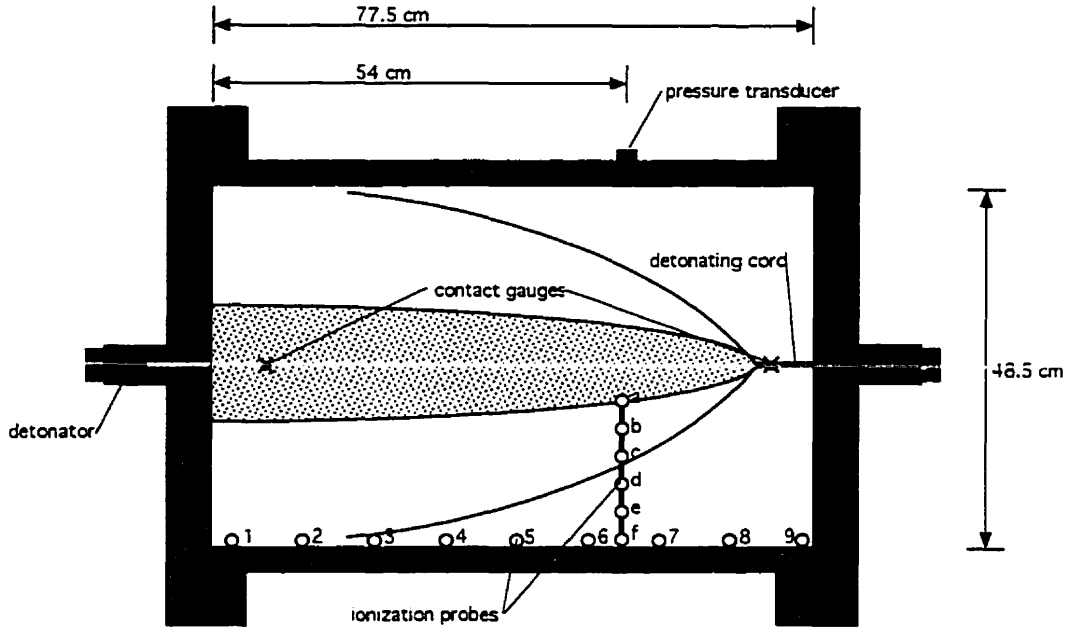

Fig. 3.3 Experiment schematic

3.3 Mixture Selection and Preparation

The experiments were performed in acetylene-air, hydrogen-air and ethylene-nitrogen-oxygen mixtures at room temperature and initial pressure of 0.33, 1, and 3 bar. These mixtures were chosen for their well-documented detonation cellular sizes. The detonation cell size λ of the different mixtures investigated is documented in Appendix A. The bottled gases used were of 99.5% purity. Bottled dry air was used to eliminate humidity effects. The combustible mixtures of interest were prepared by the partial pressure technique (i.e. for a given volume, the partial pressure of the components represents their molar concentration). To prepare a chosen mixture, the chamber was first evacuated to less than 1 Torr using an Edwards (2 stage # 40) vacuum pump. In order to minimize leaks, the component with the highest molar concentration was first bled into the chamber until the desired partial pressure was reached. The other components were introduced successively until the desired total pressure of the mixture was obtained. The pressures were accurately measured with a digital static pressure transducer (MKS-122A) to $\pm$ 0.1 Torr. For test mixtures at an initial pressure of 3 bar, a Heise pressure gauge accurate to 1 Torr was used.

Once the gaseous components were introduced into the chamber to yield the desired mixture composition, a bellows-type re-circulation pump mixed the contents in a re-circulating loop. The re-circulation was performed for a minimum of 30 minutes to ensure adequate mixing.

3.4 Diagnostics

The results of each experiment were monitored with contact gauges, ionization probes, and pressure transducers. The instrumentation is shown in Fig. 3.3. Two time-of-arrival contact gauges placed directly on the cord gave a measurement of the detonation velocity in the high explosive (PETN) cord. These contact gauges also provided a timing reference to correlate the position of the detonation in the cord with the events in the surrounding combustible gas. Ionization probes were mounted along the chamber wall (probes 1 to 9 in Fig. 3.3) at 10 cm intervals, and on a radial sting (probes *a* to *f* in Fig. 3.3) perpendicular to the wall (3-4 cm intervals). These probes tracked the time of arrival of the combustion front in the gaseous mixture at the various fixed probe locations. The ionization probes consisted of two thin copper electrodes separated by a 1-mm gap. A signal is obtained upon passage of the ionized combustion front, which closes the circuit. A piezoelectric pressure transducer mounted on the chamber wall gave a measure of the strength and time of arrival of the generated shock wave (or detonation). The signals from the contact gauges, ionization probes and pressure transducers were recorded on a LeCroy digital oscilloscope.

3.5 Reduction of Velocity Measurements

The radial and axial phase velocities V_R and V_X of the combustion wave in the gaseous mixture were obtained from the time-of-arrival of the combustion front at the fixed radial and axial probe location (c.f. Fig. 3.3). An explanatory sketch of the measured phase velocities is given in Fig. 3.4. The velocities were determined at the mid-point between two successive ionization probes. The characteristic error in these velocity measurements is estimated to be ±5%. The measurements

of V_x permitted us to verify if the generated wave "translates" along the direction of the cord at the detonation velocity in the cord V_{DC}.

As was shown in Chapter 2, beyond the immediate vicinity of the cord, the shock inclination angle δ_s is small (the quasi-cylindrical assumption). The difference between the radial velocity V_R and the normal velocity of the wave V is very small and within the experimental error. The measurements of V_R thus permit us to differentiate between the different regimes of initiation. In the supercritical regime, the blast wave decays to the constant Chapman Jouguet detonation velocity V_{CJ}. In the other limit of the subcritical case, the combustion front de-couples from the shock and decays to a weak shock. Oscillations in the measurements of V_R indicate the unstable critical regime of direct initiation.

It should be noted that in a small chamber, detonation can also be initiated by the reflection of blast wave on the chamber wall. However, this can be differentiated from direct initiation by the detonating cord by examining the direction the combustion front propagates along the radial sting.

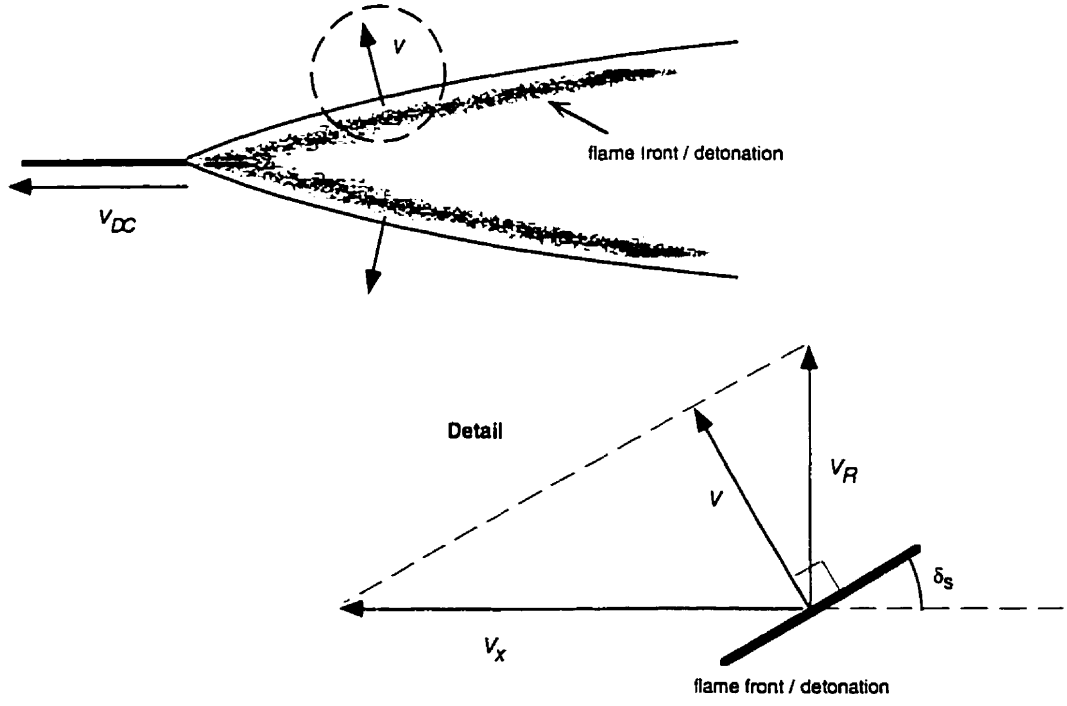

Fig 3.4 Combustion wave phase velocities

3.6 Results

3.6.1 Acetylene-air mixtures

The first set of experiments was carried out in stoichiometric acetylene-air mixtures. The velocity of the reaction front in the radial direction is shown in Fig. 3.5. Within 10 cm from the cord, the combustion front has already decayed to the CJ detonation velocity of the mixture. The detonation front propagated steadily at the CJ velocity thereafter until it reached the chamber wall. The recorded pressure (~20-40 bar) as the wave impacted the wall corresponds to that of a detonation wave. The time of arrival of the combustion front at the wall coincided with the shock wave arrival time as measured by a pressure transducer at that same radial location. This demonstrates that the shock front and combustion wave are coupled.

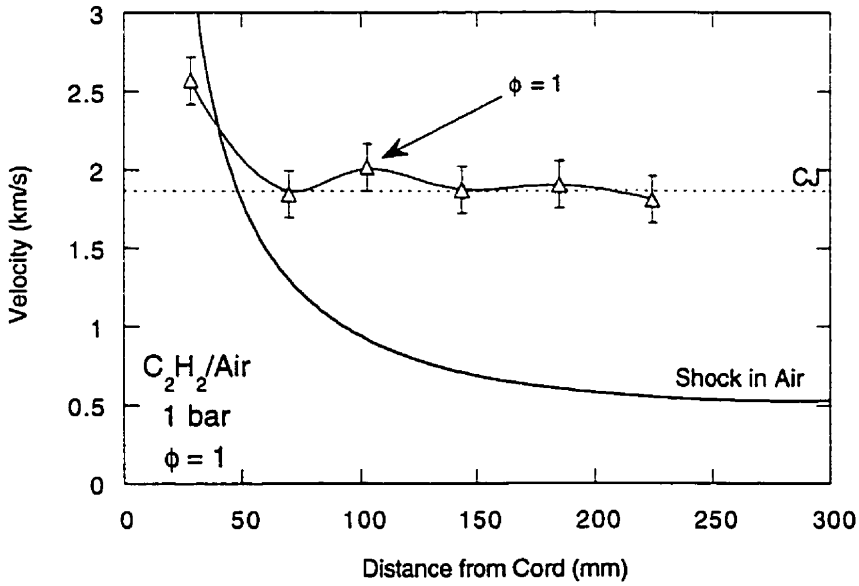

Fig. 3.5 Radial velocity profile for stoichiometric acetylene-air

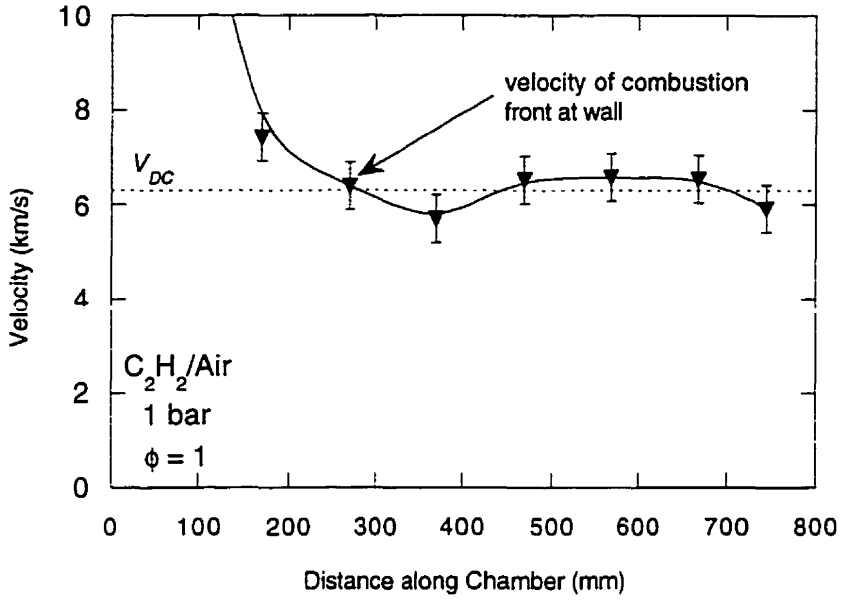

Fig. 3.6 Axial velocity profile for stoichiometric acetylene-air

The velocity of the reaction front in the axial direction measured along the chamber wall is shown in Fig. 3.6. The result indicates that the reaction front moved along the wall at constant velocity, equal to the detonation speed in the PETN detonating cord (6.3 km/sec). The fluctuations are within the experimental error.

The results of Fig. 3.5 and 3.6 indicate that a conical detonation is directly initiated, in which the combustion front and the shock are coupled. This corresponds to the supercritical regime of initiation. Using the axial and radial phase velocities of the combustion wave, the detonation wave angle can be obtained:

$$\theta = \tan^{-1}\left(\frac{V_R}{V_X}\right) \approx \tan^{-1}\left(\frac{1.8\,\text{km/s}}{6.3\,\text{km/s}}\right) \approx 17^\circ \qquad 3.1$$

in good agreement with theoretical predictions.

3.6.2 Hydrogen-Air Mixtures

Further investigation of direct initiation by detonating cord was performed in a less sensitive mixture (hydrogen-air), where the energy liberated by the cord approaches the critical energy of initiation. The mixture sensitivity was varied via the fuel equivalence ratio. The radial velocity profiles of the combustion front are shown in Fig. 3.7 for a wide range of fuel equivalence ratios at an initial pressure of 1 bar. For comparison, the non-reacting blast wave velocity decay in air is also shown. For the most sensitive mixture ($\phi = 1$), the velocity profile was initially overdriven but quickly decayed to the CJ velocity of the mixture. This result is similar to the previous supercritical case for acetylene-air (Fig. 3.5). As the mixture sensitivity was decreased (by reducing the fuel equivalence ratio ϕ), the velocity profile became more irregular. For an equivalence ratio of $\phi = 0.75$, the velocity of the combustion front demonstrated large fluctuations, characteristic of the critical regime. For an equivalence ratio of 0.7, the combustion front decayed from near CJ velocity to ~1 km/sec. For even leaner hydrogen mixtures, a combustion front was no longer recorded. However, detonation initiation by the reflection of the decayed blast wave off the chamber wall was sometimes observed near these critical conditions.

The results for the velocity profile of the combustion front measured in the direction of the detonating cord (V_x) along the chamber wall are shown in Fig. 3.8. For an equivalence ratio of $\phi = 1$, the velocity profile was fairly constant, corresponding to the detonation velocity in the cord (i.e. 6.35 km/s). As the mixture became less sensitive ($\phi = 0.8$), the velocity profile exhibited increasing fluctuations. However, the average velocity of the front was still approximately the detonation velocity in the cord. The fluctuations in the combustion front velocity along the cord indicate that the conical detonation was subject to increasing instabilities and became more irregular near the critical initiation condition. If the mixture sensitivity was further reduced ($\phi = 0.75$), significant oscillations were observed in the velocity profile. The arrival time of the combustion front along the chamber wall is no longer synchronized to the detonation in the cord. The fluctuations of the velocity profile near critical

conditions suggest the presence of stochastic, asymmetric initiation events due to local hot spots.

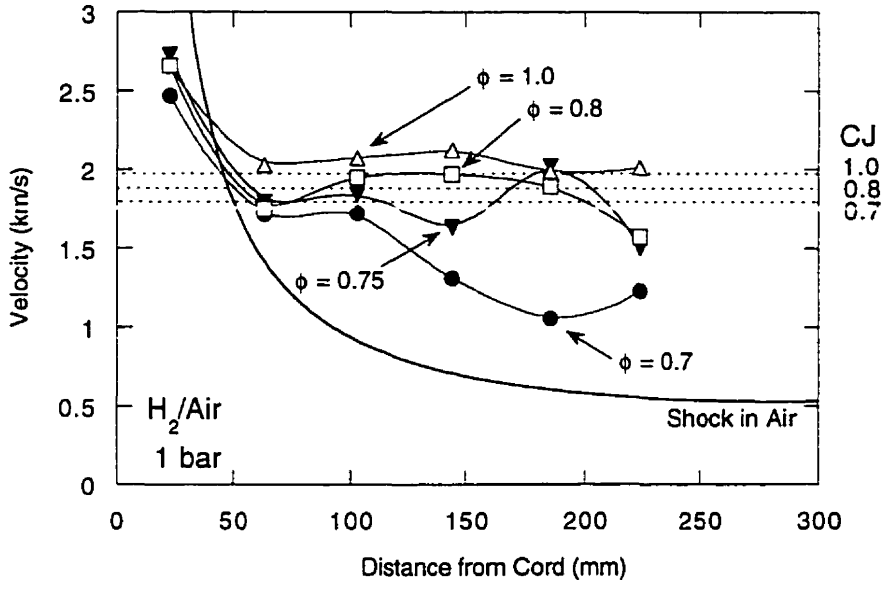

Fig. 3.7 Radial velocity profile in hydrogen-air mixtures

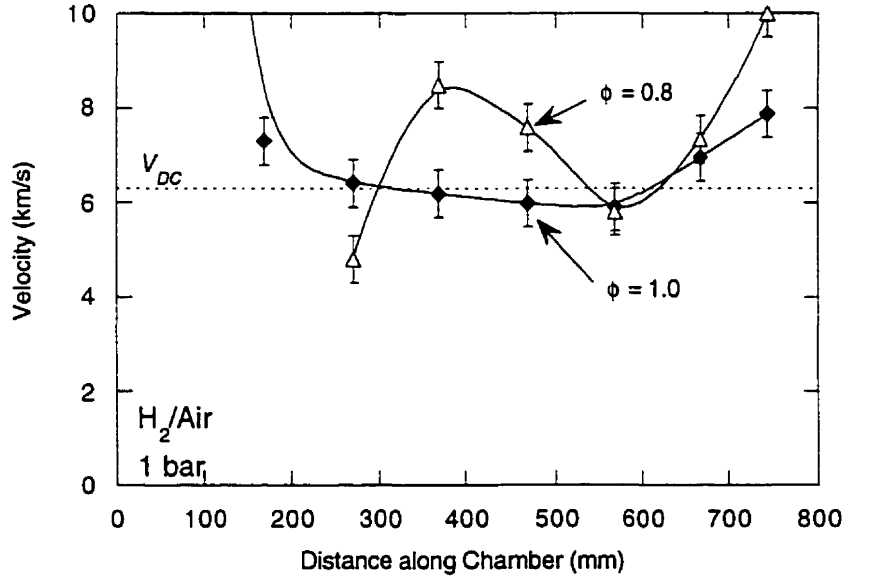

Fig. 3.8 Axial velocity profile in hydrogen-air mixtures

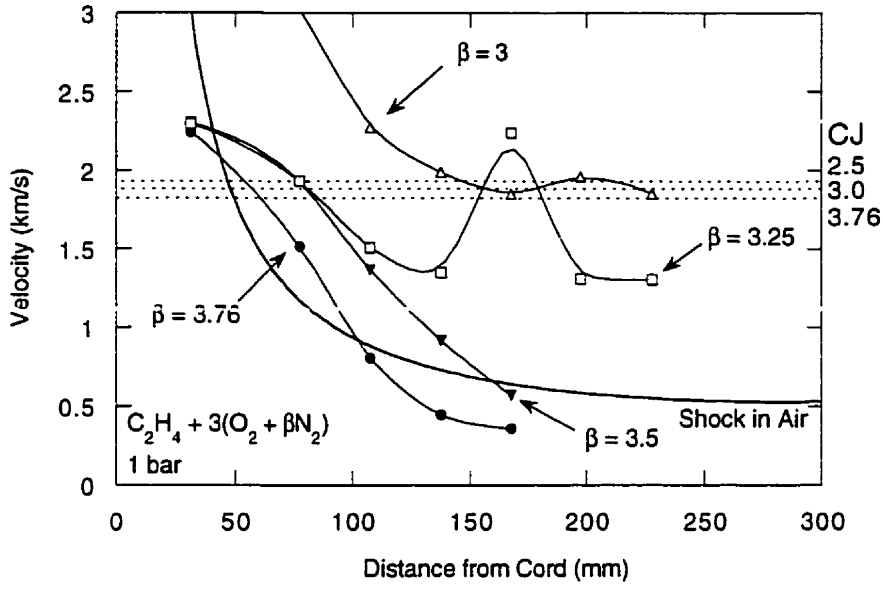

Fig. 3.9 Radial velocity profile in ethylene-oxygen-nitrogen mixtures, P_O = 1 bar

3.6.3 Ethylene-Oxygen-Nitrogen Mixtures

Experiments on the initiation of stoichiometric ethylene-oxygen mixtures at 1 bar initial pressure with various values of the nitrogen/oxygen dilution ratio β (i.e., $C_2H_4 + 3(O_2 + \beta N_2)$) were also carried out. The same strength of detonating cord (30 kJ/m) was used. The results of the velocity of the combustion front are shown in Fig. 3.9 for the range of nitrogen dilution varying between β = 3 and 3.76 (air). Here, the addition of the inert nitrogen decreases the sensitivity of the mixture. For stoichiometric ethylene-air (β = 3.76), the combustion front decoupled from the shock and decayed to a very low velocity (~ 400 m/sec), typical of the subcritical regime. As the mixture was made more sensitive by decreasing the amount of nitrogen dilution to β = 3.5, detonation initiation was still not observed. For a further reduction to β = 3.25, the combustion front decayed to approximately 60% of the Chapman-Jouguet value of the mixture. At approximately 13 cm from the detonating cord, the wave exhibited a large oscillation to super-CJ velocity, after which the wave eventually decayed to a low sub-CJ velocity of approximately 1.6 km/s. The velocity fluctuations of the

combustion front are indicative of conditions near the critical regime of initiation. Further reduction of the amount of nitrogen dilution to $\beta = 3$ resulted in successful direct initiation. The combustion front decayed asymptotically to the Chapman-Jouguet velocity of the mixture. For this mixture, the distinction between the supercritical and subcritical regimes was more definitive than for hydrogen-air mixtures. This is due to the fact that in ethylene mixtures the ionization in the combustion front is greater than in hydrogen mixtures. The signals from the ionization probes may thus be obtained in the limit of the subcritical regime, where the combustion region is less intense.

So far, all the experiments have been conducted at 1 bar initial pressure with the same detonating cord strength. Further experimentation can be performed with detonating cords of different strengths. However, for higher energy cords, the blast wave will be stronger at a larger distance from the cord, thus rendering the present chamber size too small. Although weaker detonating cords are available, the inert coating on the cord will begin to have a more pronounced effect on the effective energy deposition. Therefore, to decrease the blast effect for the same detonating cord, the initial pressure of the gaseous mixture can be increased. This would have the effect of lowering the *effective* strength of the cord, which is reflected by the explosion length scale $R_0 = (E_s/P_0)^{1/2}$.

The results obtained for a stoichiometric ethylene-oxygen mixture with variable nitrogen dilution at an increased initial pressure of 3 bar are shown in Fig. 3.10. These results show the velocity of the combustion front for various amounts of nitrogen-oxygen dilution β. The distinction between "go" and "no-go" is very sharp. For nitrogen dilutions of $\beta = 3.76$ (air) and 3.7, the combustion front velocity decayed to approximately 100 m/sec before reaching the chamber wall. This decay resembles the profile of a decaying blast in an inert gas. This clearly corresponds to the subcritical regime of initiation, where the shock and combustion front are de-coupled. By reducing the amount of nitrogen dilution below $\beta = 3.45$, the mixture became sufficiently sensitive to permit direct initiation of detonation. Within 5 cm from the source, the blast wave was seen to have decayed to the CJ velocity of the mixture.

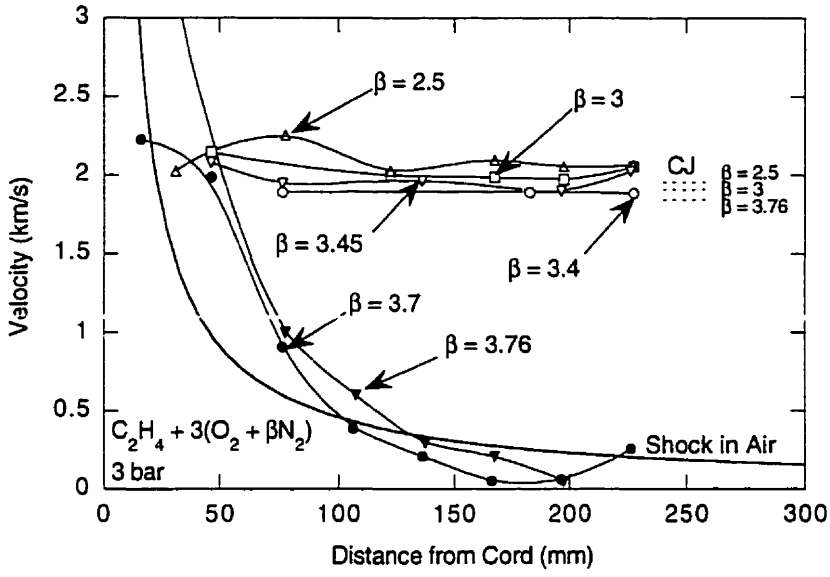

Fig. 3.10 Radial velocity profile in ethylene-oxygen-nitrogen mixtures, $P_O = 3$ bar

Further investigation of the effects of initial pressure was pursued in the same nitrogen-oxygen-nitrogen system at an initial pressure of 0.33 bar. The radial velocity profiles are shown in Fig. 3.11. Care must be exercised in interpreting these results, since the increase of the effective energy of the cord now gives a longer overdrive of the blast wave. This makes the distinction between "go" and "no-go" difficult within the small size of the blast chamber used in the present study. However, the "stretching out" of the initiation phenomena over greater distances permits a higher resolution examination of the flow field closer to the cord (i.e. in the regions pertinent to the onset of detonation). The nitrogen-oxygen dilution ratio β was varied between 2 and 3.5. For all cases, the combustion front decayed close to the CJ value of the mixture within 10 cm from the cord. The combustion front then propagated at this velocity in a quasi-steady manner for ~5 cm, after which two outcomes were observed. For nitrogen dilution ratios less than 2.5, the front continued to propagate further at velocities close to CJ, suggesting that a detonation wave had been initiated. For β less than 3, the combustion front abruptly decayed to less

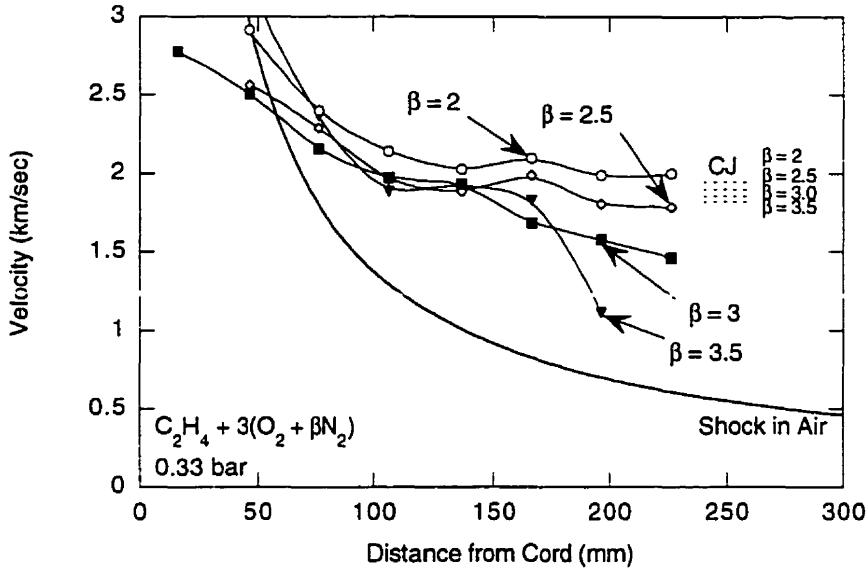

Fig. 3.11 Radial velocity profile in ethylene-oxygen-nitrogen mixtures, $P_o = 0.33$ bar

than 1.5 km/s. In these cases, it is difficult to conclusively assess whether re-initiation would have occurred if the chamber size were bigger. However, in view of the results presented above, these sub-CJ velocity excursions clearly indicate near limit, critical behavior.

3.7 Discussion of Results

The results for the supercritical regime of initiation obtained for hydrogen-air and ethylene-oxygen-nitrogen are consistent with the results obtained above for acetylene-air. The flow field consists of a blast wave that decays to the Chapman Jouguet velocity of the mixture and then propagates steadily at this velocity. The axial velocity measurements confirm that the flow is steady and translates along the axis of the cylindrical chamber at the detonation velocity of the PETN in the cord.

In the subcritical regime, the initially overdriven shock wave near the cord fails to couple with the combustion front and decays to a low velocity before reaching the chamber wall. This is analogous to the de-coupling between blast

and combustion front in the classic schlieren pictures taken by Struth *et al.* (1963) in the sub-critical regime of projectile inititiation, shown in Fig. 3.12.

In the critical regime, the flowfield is not amenable to such a simple interpretation. In the early stages of blast decay, the shock and combustion front coincide, since the wave is overdriven and the blast energy of the source dominates the shock propagation mechanism. After the wave has decayed to a velocity slightly below CJ velocity, the shock trajectory departs from the theoretical non-reacting blast wave trajectory as the influence of chemical heat release starts to influence the blast motion. The combustion front continues to propagate at a constant velocity of approximately 0.5 - 1 V_{CJ} for a short period, followed by oscillations. This behavior is similar to the velocity profiles of the combustion front measured by Edwards *et al.* (1978) and Elsworth *et al.* (1979) for spherical initiation using microwave interferometry. These oscillations, with apparent radial velocities above the CJ value, are indicative of three dimensional

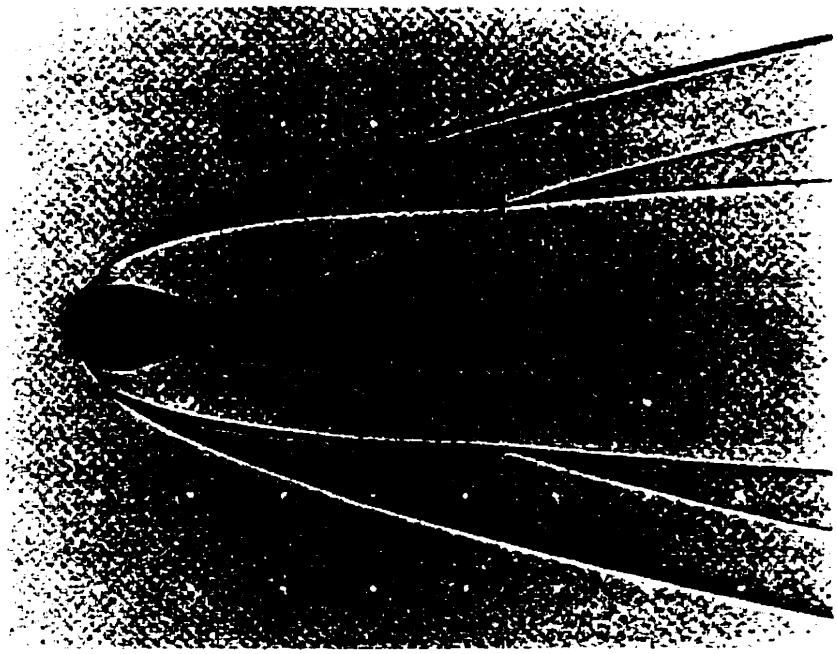

Fig. 3.12 Bow shock wave and combustion front generated by a 9 mm sphere fired into a stoichiometric hydrogen-air mixture (P_O = 0.55 atm, V_{sphere} = 2870 m/s), from Struth, Behrens and Wecken (1963)

explosion centers. The non-sequential time of arrival of the measured combustion front on the chamber wall indicates that these explosion centers are stochastic.

A summary of the results reported above for hydrogen/air mixtures at 1 bar and stoichiometric ethylene-oxygen mixtures with variable nitrogen dilution at 0.33, 1, and 3 bar initial pressure is given in Table 3.1. The effective strength of the cord is represented by the explosion length $R_O = (E_S/P_O)^{1/2}$. The critical radius R_S^* at the termination of the quasi-steady regime and before the onset of any fluctuation is given for each critical mixture. The cell sizes λ corresponding to the critical mixture compositions determined experimentally are taken from the literature. The variation of the cellular size with mixture composition is given in Appendix A.

Table 3.1 Summary of results for critical direct initiation by detonating cord of fixed strength

	$H_2 - Air$	$C_2H_4 - O_2 - N_2$, $\phi = 1$	$C_2H_4 - O_2 - N_2$, $\phi = 1$	$C_2H_4 - O_2 - N_2$, $\phi = 1$
	1 bar	1 bar	0.33 bar	3 bar
E_S	30 kJ/m	30 kJ/m	30 kJ/m	30 kJ/m
$R_O = (E_S/P_O)^{1/2}$	55 cm	55 cm	95 cm	32 cm
Critical Mixture	$\phi = 0.7 - 0.8$	$\beta = 3.0 - 3.5$	$\beta = 2.5 - 3$	$\beta = 3.5 - 3.76$
R_S^*	10 ± 2 cm	14 ± 2 cm	16 ± 2 cm	5 ± 1 cm
$\lambda^*_{exp.}$	2.3 ± 0.5 cm	2.2 ± 0.4 cm	3.6 ± 1 cm	0.9 ± 0.2 cm
$R_S^* / \lambda^*_{exp.}$	4.3	6.4	4.4	5.6
$(E_S^*)_{Lee}$	18 ± 9 kJ/m	20 ± 8 kJ/m	18 ± 15 kJ/m	10 ± 5 kJ/m
$(E_S^*)_{Vasilev}$	11 ± 5 kJ/m	12 ± 5 kJ/m	11 ± 7 kJ/m	6 ± 3 kJ/m

3.8 Comparison with Lee-Vasil'ev Theory of Initiation

The problem of detonation initiation by hypersonic projectiles, or by rapid energy deposition along a line, has been addressed recently by the theories of Lee (1997) and Vasil'ev (1994). Their work is based on the blast wave analogy for hypersonic flows. For a successful initiation of detonation, Lee argues that the energy deposited in the reacting mixture by the projectile should at least equal the critical energy per unit length necessary to initiate a cylindrical detonation wave.

In Chapter 2, it was shown that the flowfield around the detonating cord could be accurately approximated as quasi-cylindrical beyond the immediate vicinity of the cord. Since the onset of detonation occurs well beyond the immediate vicinity of the cord, the flowfield in the combustible gas is quasi-cylindrical in the region pertinent to detonation initiation. The question, "Will the cord directly initiate detonation?" translates into, "Is the energy per unit length of the cord enough to initiate a cylindrical detonation?"

For purely cylindrical initiation, the functional relationship for the critical energy in terms of the initial conditions and mixture sensitivity has the form (Lee, 1997):

$$E_s^* \equiv k\gamma P_o M_{CJ}^2 \lambda^2 \qquad 3.2$$

where λ is the detonation cell width. Unfortunately, at present there is no way to predict the constant k from purely theoretical considerations. To estimate the value of k, Lee suggests that the initiation energy must be of sufficient strength so that when the blast wave has decayed to half the CJ velocity (the auto-ignition limit of the mixture), the blast wave has reached some critical radius R_s^*. Lee argues that a value $R_s^* = 3.2\lambda$ is appropriate, based on the critical slot width (the two-dimensional analog of the critical tube diameter) necessary to initiate a cylindrical detonation. The critical energy estimate of Lee becomes

$$E_s^* \equiv 10.1\gamma P_o M_{CJ}^2 \lambda^2 \qquad 3.3$$

Based on the cellular structure directly, the empirical model of Vasil'ev (1994) yields an estimate for the critical initiation energy of a multi-front cylindrical detonation E_s^* in terms of the "re-initiation energy" in an individual elementary cell E_o (Vasil'ev and Nikolaev, 1978)

$$E_s^* = nE_o \approx n\ 0.22\rho_o D_{CJ}^2 l^2 \qquad 3.4$$

where l is the length of an elementary cell. The proportionality coefficient n is estimated from experiments on detonation emergence from a slot. The expression for critical energy becomes

$$E_s^* \equiv 2.3\rho_o D_{CJ}^2 l^2 \qquad 3.5$$

Using the general relationship $l = 1.6\lambda$ relating cell width and cell length, and noting that the initial density can be expressed as $\rho_o = \gamma P_o / c_o^2$, Eq. 3.5 can be re-arranged as:

$$E_s^* \cong 5.9\gamma P_o M_{CJ}^2 \lambda^2 \qquad 3.6$$

In Table 3.1, the critical energy estimates of Lee and Vasil'ev (Eqs. 3.3 and 3.6) corresponding to the experimentally determined critical mixture compositions (i.e. the critical value of λ) are given for comparison with the actual energy liberated by the detonating cord (30 kJ/m). The accuracy of the experimentally determined critical conditions is reflected in the critical cell size, and therefore in the theoretical predictions of critical energy. Clearly, both theoretical estimates predict the correct order of magnitude for the critical source energy required to directly initiate a cylindrical detonation.

There is some disagreement in the literature on the critical radius at which initiation occurs. Estimates of the critical radius vary widely, from 3λ to 20λ (Lee, 1997, Aminallah et al., 1993). The present results help to clarify this discrepancy. The critical radius R_s*, defined above as the radius at which the combustion front, after a quasi-steady period, either decays (subcritical regime) or exhibits oscillations (critical regime) indicates where the source energy is replaced by the chemical energy of gas combustion in driving the blast wave. The critical radius of initiation occurs at approximately 4 to 6λ for the mixtures used here.

3.9 Concluding Remarks

Although the detonating cord is not a perfect source for cylindrical initiation due to the finite detonation velocity in the cord, the experimentally determined critical conditions appear to agree with those predicted by theories of cylindrical initiation. This agreement supports the idea that the initiation characteristics of the detonating cord can be quantified by the energy release per unit length.

The details of the initiation process in the critical case, however, do not appear to have the symmetry associated with cylindrical initiation. Although the supercritical case appears to be symmetric, resulting in a steady conical flow field,

the results in the critical regime are more consistent with local events, such explosion centers.

Chapter 4 Large Scale Investigation of Detonation Initiation by Detonating Cord

4.1 Overview

The range of conditions in the experiments reported in the last chapter were limited by the size of the blast chamber. Measurements of the combustion wave velocity profile could only differentiate between the different initiation regimes. Particularly, only limited information could be obtained regarding the onset of detonation in the critical regime of initiation. In the present chapter, the study of initiation of quasi-cylindrical detonations is extended to a wider range of source energies in order to provide a better assessment of blast initiation theory. The present experiments were performed in large transparent plastic bags, which permitted high-speed photographic observation of the phenomenon, particularly of hot spot formation near the critical regime.

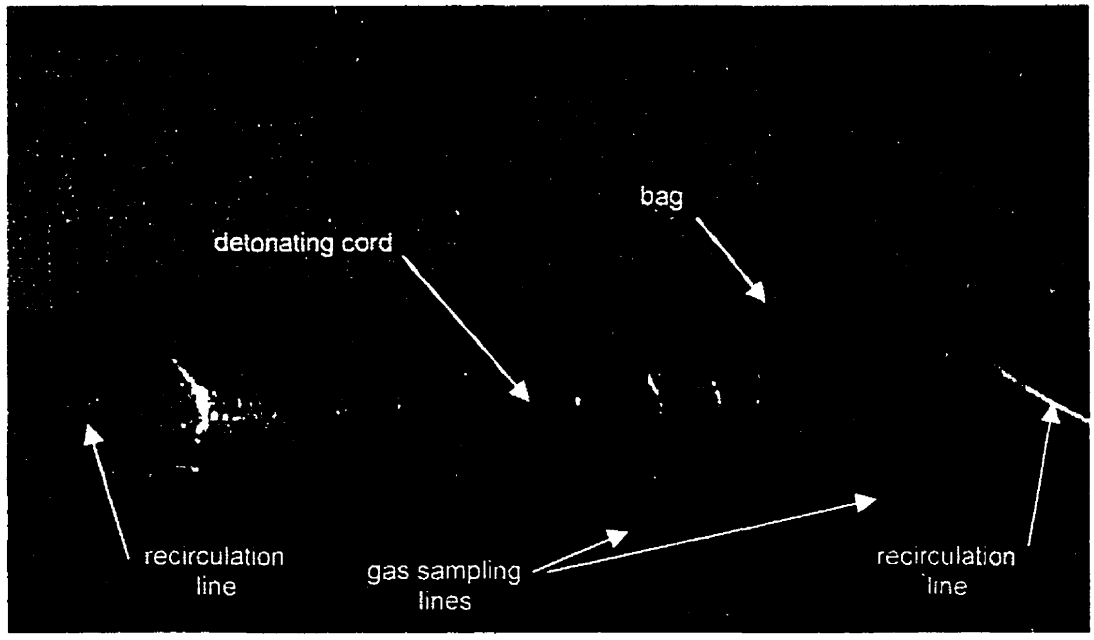

Fig 4.1 Picture of bag set-up (DRES)

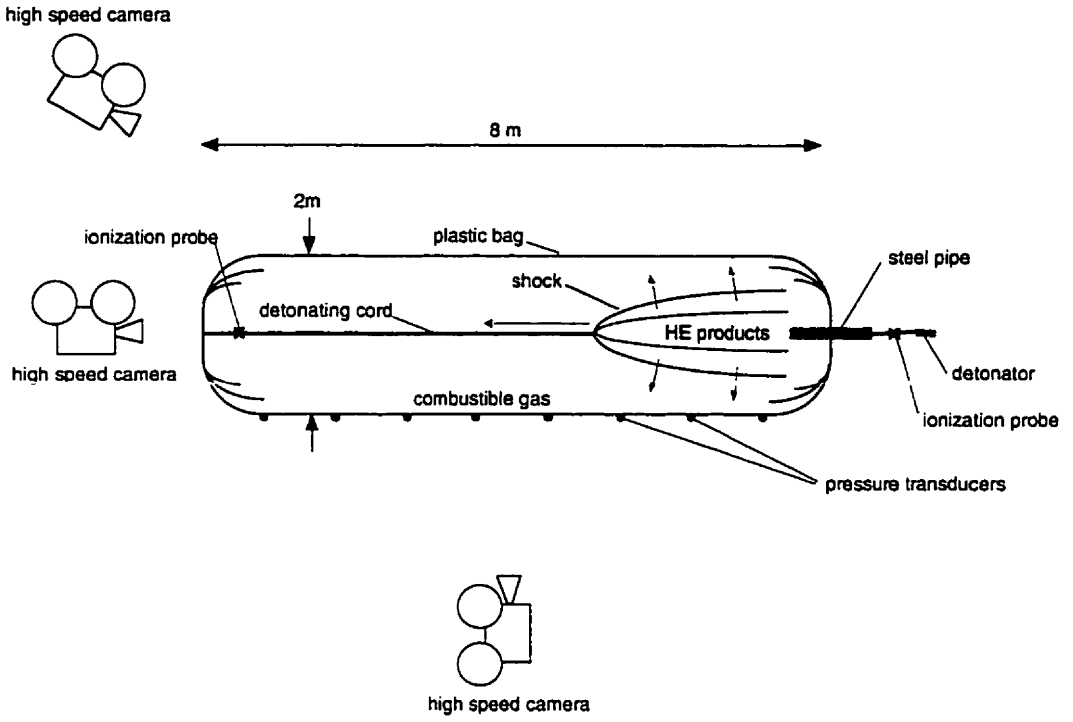

Fig. 4.2 Experiment and instrumentation schematic

4.2 Experimental Details and Procedure

The large-scale field experiments were performed at the Defence Research Establishment Suffield (DRES), Alberta, Canada. Large 8-m-long and 2-m-diameter thin-walled plastic bags filled with combustible gas were used (Fig. 4.1). The larger diameter bags allowed higher energy detonating cords to be used than those used in the 0.5-m-diameter chamber in the study reported in Chapter 3. The PETN detonating cords used in these experiments had nominal core loadings of 50, 70, 200, and 400 gr./ft, yielding energies of 65, 91, 260, and 520 kJ/m respectively[1]. The detonating cord was positioned axially inside the bag, running along the bag's entire length. To prevent sagging due to gravity, one end of the detonating cord was attached to an elastic band. The detonating cord was initiated at the other end by a Reynolds detonator placed outside the bag. The first 0.9 m of the detonating cord was confined by a strong steel pipe to prevent any interaction between the blast wave from the cord and the support structure when

[1] The amount of energy deposition by the cord is taken from the heat of detonation of PETN, 6.332 kJ/g (taken from Dobratz and Crawford, 1985)

the detonation in the cord enters the bag. A schematic of the experimental set-up is shown in Fig. 4.2.

The experiments were conducted at ambient atmospheric conditions (0.92 bar, 10-20 °C). Ethylene (C_2H_4) was used as the fuel for all the tests. Air at atmospheric conditions was used as the oxidizer. The mixtures were prepared by continuous re-circulation of the mixture inside the inflated bag. Fuel was injected periodically until the desired concentration was reached. The composition of the mixture was monitored by an infrared mass spectrometer (Wilks Miran 80) via continuous sampling. This system guaranteed the mixture concentration to within ±0.05% ethylene in air. After a uniform and stable mixture was obtained, the re-circulation fan was stopped before firing. For a full description of the large-scale facility at DRES, the reader is referred to Funk and Murray (1982) and Murray (1984).

4.3 Diagnostics

Each experiment is monitored by ionization probes, pressure transducers and high speed cameras (c.f. Fig. 4.2). Ionization probes placed directly on the cord measured the time of arrival of the detonation in the PETN at the fixed probe location. These measurements also provided a timing reference with the events in the surrounding combustible gas. Piezoelectric pressure transducers mounted 1 m apart along the pad floor measured the strength and time-of-arrival of the generated blast wave (or detonation). The different times of arrival of the detonation along the cord and the blast wave at the pressure transducers on the floor permitted measurement of: *a)* the detonation velocity in the PETN cord, *b)* he average shock velocity from the cord to the pad floor, and *c)*, the velocity of the shock as it sweeps along the bag. These results are tabulated along with explanatory sketches in Appendix B.

Self-luminous high-speed video and cinematography with side-on and end-on views (c.f. Fig. 4.2) were used for the visualization of the flow field. The high-speed cinematography and video, with maximum framing rates of 7000 fr/sec and 1000 fr/sec respectively, captured the self-luminous combustion front in the gaseous mixture and the detonating cord products. This technique

does not permit direct observation of the shock wave in the gaseous mixture. Observation of the shock would require shadowgraph/schlieren photography, which are extremely difficult to implement in large scale field trials.

4.4 Results

4.4.1 The Subcritical Regime

As the detonation in the high explosive cord emerges from the confining pipe and enters the bag, the expansion of the high explosive products drives a blast wave in the surrounding combustible gaseous mixture (c.f. Fig. 4.2). Chemical reactions are triggered by the shock. If the shock is too weak, the chemical reactions fail to couple with the shock. This is the "subcritical" regime of initiation, where the energy release by the cord is insufficient to initiate detonation. A typical photographic result of the subcritical regime is shown in Fig. 4.3, where the cord energy of 520 kJ/m was insufficient to initiate detonation in an ethylene-air mixture of equivalence ratio of $\phi = 0.67$. The high-speed film captured the detonating cord products (orange-red in the photographic records) but failed to register the less intense gaseous reaction induced by the decaying shock. The non-reacting shock is not directly visible.

On the subcritical records, it can be seen that the high explosive (HE) products expand radially, forming a slender body of revolution that translates

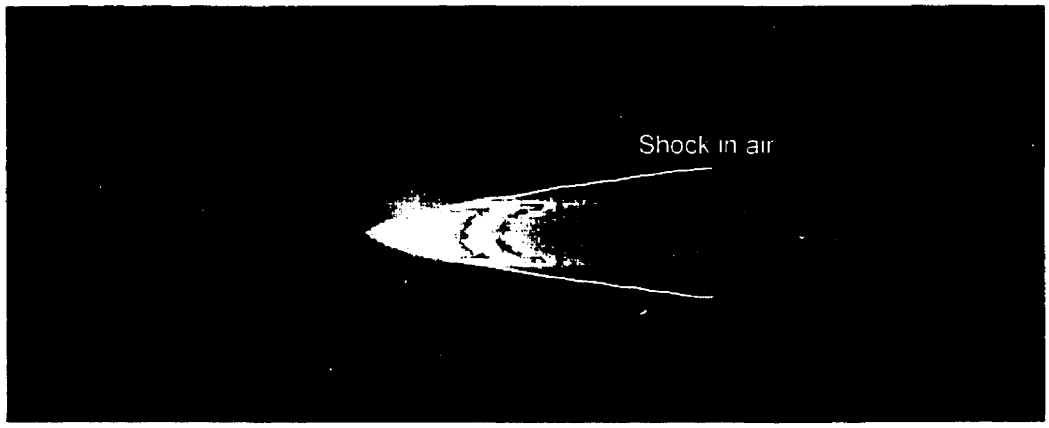

Fig 4.3 Subcritical regime in C_2H_4 – Air (Shot 39, $\phi = 0.67$, $E_S = 520$ kJ/m)

along the length of the cord at the detonation velocity in the PETN (V_{DC} = 6.5 km/s). Here, the analogy between initiation by detonating cord or by hypervelocity projectile is clearly evident in these photographs. The HE products can be viewed as a hypersonic slender projectile traveling through the bag at V_{DC} = 6.5 km/s. In the immediate vicinity of the cord, where the blast wave driven by the HE products is very strong, the shape of the shock is inferred by the shape of the hypersonic detonating cord products themselves. Beyond this initial overdrive, the shock decays similarly to a shock in air. The pressure signals obtained when the shock has reached the bag boundary indicate that the strength of the shock wave is weak. The shock average velocity between the detonating cord and the pressure transducers on the pad floor is approximately 1.6 km/s (c.f. Appendix B).

Although not visible in the photographic records, the shape of the decaying shock in the subcritical regime of initiation can be estimated by the theoretical shape of a decaying shock in air. In Chapter 2, the shock shape was measured for different strengths of detonating cord, and the results were shown to scale with the explosion length for the cylindrical geometry $R_O = (E_S/P_O)^{1/2}$. Thus, the shock shape for the different strengths of cord can be obtained from the previous results of weaker cords by the appropriate energy scaling. The estimated shock shape is shown superimposed on the image of the subcritical result of Fig 4.3. In the vicinity of the cord, the shock shape almost coincides with the shape of the expanding products. This clearly supports the conclusions reached in Chapter 2 on the velocity and inclination angle of the shock near the cord, where the blast decay is governed by the piston effect of the expanding detonating cord products.

To elucidate the parallel between the non-reacting blast and the reacting blast in the subcritical regime of initiation, an experiment was also conducted in air for the same strength of cord. The average shock velocity from the detonation front in the cord to the pressure transducers on the pad floor was 1.4 km/s. This shock velocity is only about 13% less than in the subcritical case of initiation. The slight increase in the average shock velocity for the subcritical regime as compared with the results for air indicates that the chemical heat release behind

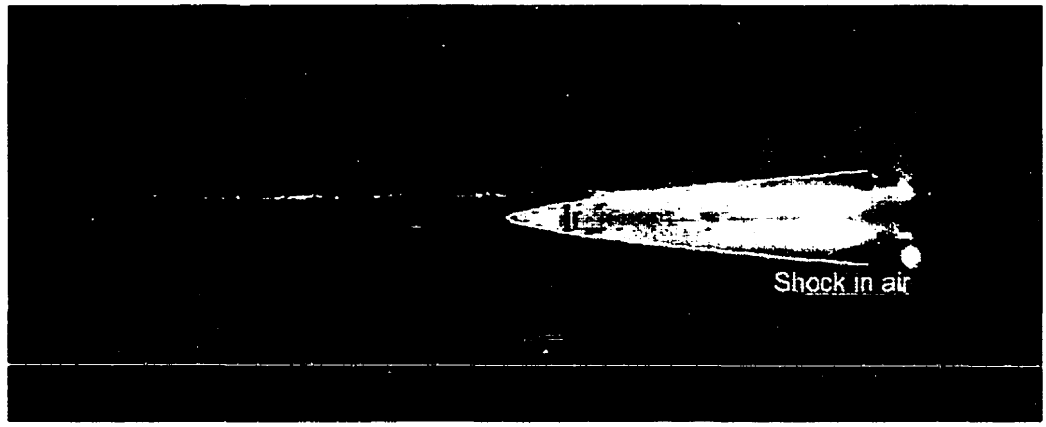

Fig 4.4 Supercritical regime in C_2H_4 – Air (Shot 52, $\phi = 1.07$, $E_S = 65$ kJ/m)

the shock slightly enhances the shock strength. This result can be explained by total energetic considerations, following the arguments of Lee *et al.* (1969): the energy engulfed by the shock in the reacting case is greater than for the non-reacting case and the chemical heat addition augments the blast front.

4.4.2 The Supercritical Regime

If the blast wave generated by the cord is sufficiently strong, the shock-induced chemical reactions in the combustible gas couple with the shock. The initially overdriven detonation near the cord decays asymptotically to a Chapman Jouguet detonation. This corresponds to the supercritical regime of initiation, when the energy release by the detonating cord is greater than the critical energy. A typical photographic record of the supercritical regime is shown in Fig. 4.4 for an equivalence ratio $\phi = 1.07$ and cord strength of 65 kJ/m. The high-speed film captures the detonation wave, which appears blue in the photographic records. The shock shape for the non-reacting case is shown superimposed on this figure for comparison. The initial overdriven blast near the cord approaches a constant angle oblique detonation wave. The half angle of the conical detonation determined from these photographic records is approximately 16°. This is consistent with theoretical arguments for steady oblique detonations, i.e.

$$\theta = \sin^{-1}\left(\frac{V_{CJ}}{V_{DC}}\right) \approx \sin^{-1}\left(\frac{1.8\,\text{km/s}}{6.7\,\text{km/s}}\right) \approx 16^{\circ} \qquad 4.1$$

and confirms that the normal velocity of the oblique wave is very close to the theoretical CJ velocity of the mixture. Moreover, the average velocity for the detonation to reach the pressure transducers on the floor is 1.8 km/s, which is very close to the Chapman Jouguet theoretical value (V_{CJ} = 1.825 km/s), as computed by the equilibrium code STANJAN (Reynolds, 1981). Subsequent frames of the same experiment show an identical flow field pattern that has been "translated" along the bag at the detonation velocity of the PETN in the cord (V_{DC} = 6.7 km/s), suggesting that the flow field is steady. The long debated stability of CJ oblique detonation waves is thus confirmed (Pratt et al., 1991, Shepherd, 1994).

Interesting observations on the cellular structure of the initiated detonation wave can also be obtained from these experiments. As the gaseous detonation reached the edge of the bag, the bag was "ripped" in thin strips. The width of these thin plastic strips which remained on the site after a supercritical experiment were found to be quite close to the cell size of the mixture (see Appendix A for the cell size λ for C_2H_4-Air mixtures). Similar observations have been obtained in previous "bag" tests (Murray and Lee, 1984). It is believed that these strips are produced by the piercing action of the triple points followed by a longitudinal shearing process.

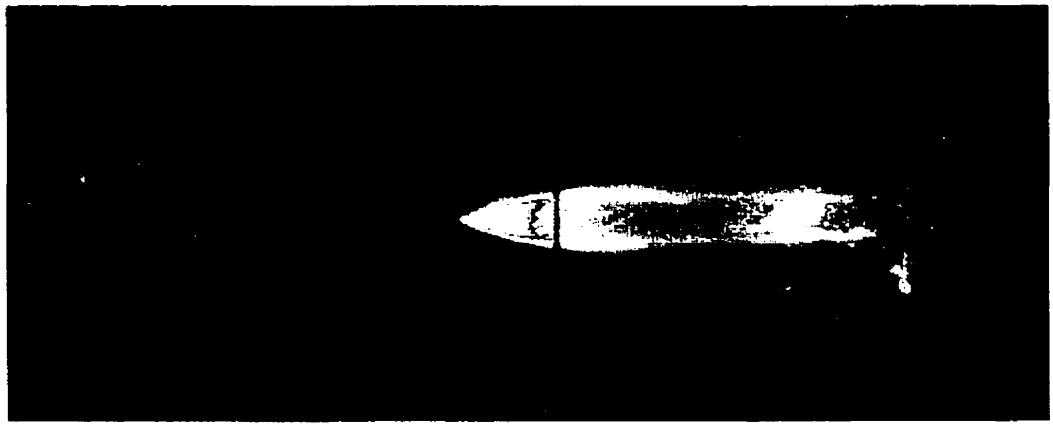

Fig 4.5 Supercritical regime in C_2H_4 – Air (Shot 36, ϕ = 0.94, E_S = 260 kJ/m)

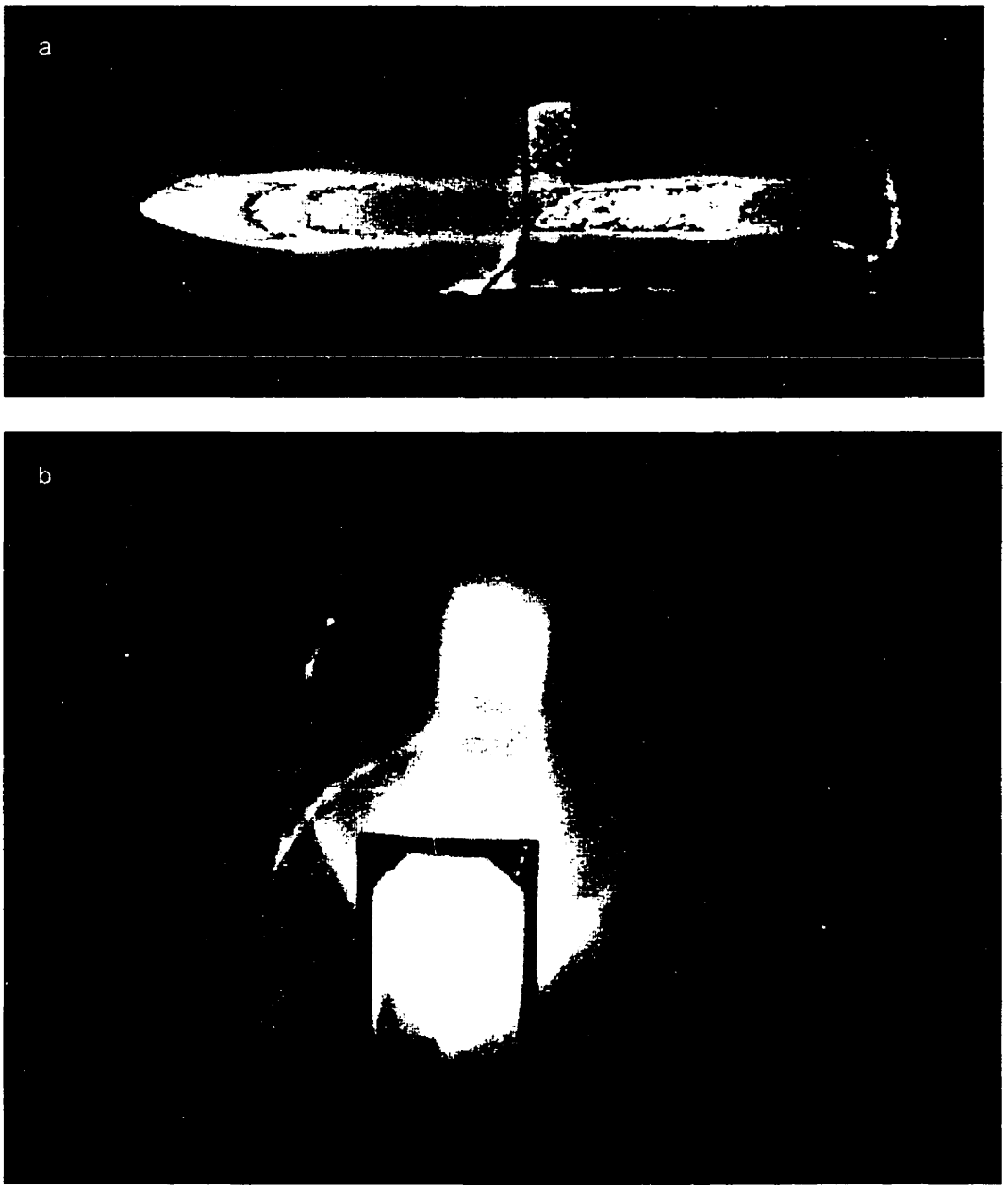

Fig. 4.6 Supecritical regime in C_2H_4 – Air (Shot 45, $\phi = 0.76$, $E_S = 520$ kJ/m), a) side view, b) top view

Repeated experiments in the supercritical regime of initiation for the different strengths of cord have yielded identical flow patterns. Side-on photographic records of experiments with different mixture compositions and detonating cord strengths are shown in Fig. 4.5 and 4.6a, for $\phi = 0.94$, $E_S = 260$ kJ/m and $\phi = 0.76$, $E_S = 520$ kJ/m respectively. It can be seen that as the strength of the detonating cord increases, the detonating cord products expand

over a larger volume, thus overdriving the blast wave over longer distances. In both experiments, the initial overdriven blast in the vicinity near the cord decayed to a steady conical Chapman-Jouguet detonation. The conical detonation can also be seen in Fig 4.6b, in a photograph taken from above.

To verify whether a true self-sustained detonation was indeed initiated in the supercritical regime, an experiment was conducted with a detonating cord abruptly ending halfway in the bag. The end of this shorter detonating cord was attached to a long elastic band. Successive frames of the detonation diffraction at the end of the cord are shown in Fig. 4.7 ($\phi = 0.98$, $E_S = 260$ kJ/m). For the first half of the bag, the detonating cord initiated a conical detonation wave, similar to the results reported above (*frame a*). After the detonating cord ended (*frame b*), an expansion originating from the end of the cord reached the detonation front and curved it (*frames c-g*). This is similar to the critical tube diameter problem, only now it is a cylindrical detonation that is diffracted laterally into a spherical one. Finally, the wave was diffracted over the entire cross-sectional span of the bag and transitioned to a nearly planar detonation propagating into unreacted gas at the CJ velocity (to the left in the photographic records).

A similar experiment was conducted to see how the detonation is diffracted when the cord initially exits the confining pipe (Fig. 4.8). This time, for the first 1.6 meters of the bag, a strong pipe confined the detonating cord. As the detonation in the cord emerged from the end of the pipe, a conical detonation wave is formed. However, the expansion originating from the start of the cord weakened the oblique detonation and curved it back. A teardrop-shaped detonation results, formed by an un-attenuated conical detonation in front and a diffracted detonation in the back (*frame d*). As the detonation in the cord continued further to the left, the teardrop grew in a self-similar manner. Eventually, as the teardrop detonation wave reached the edges of bag, the curved detonation in the back continues to propagate at nearly the CJ velocity into the unreacted mixture (to the right in the photographic record). The effect of a finite length detonating cord clearly illustrates that the gaseous detonation wave initiated by the detonating cord in the supercritical regime is a self-sustained CJ wave. The final geometry of the detonation wave is simply determined by the

experimental boundary conditions. The continuous line-source of energy (the cord) creates a quasi-cylindrical detonation. Where the line-source of energy ends (at either extremity of the cord), the detonation wave is diffracted into a curved detonation. When the detonation reaches the bag, it is further diffracted into a planar detonation which propagates down the bag.

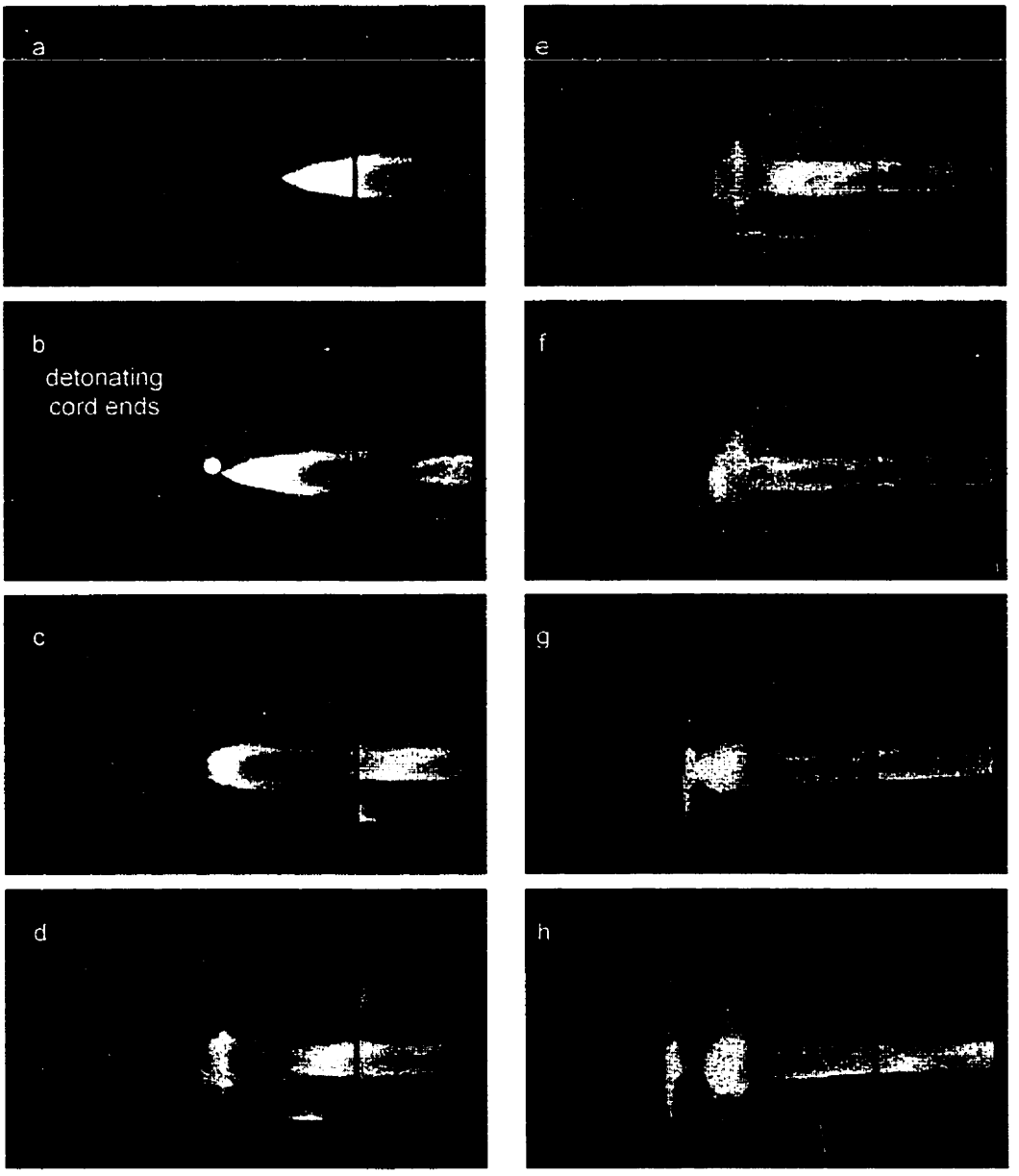

Fig 4.7 Effect of finite length of detonating cord (Shot 41, $\phi = 0.98$, $E_S = 260$ kJ/m), frames taken 143 μsec apart

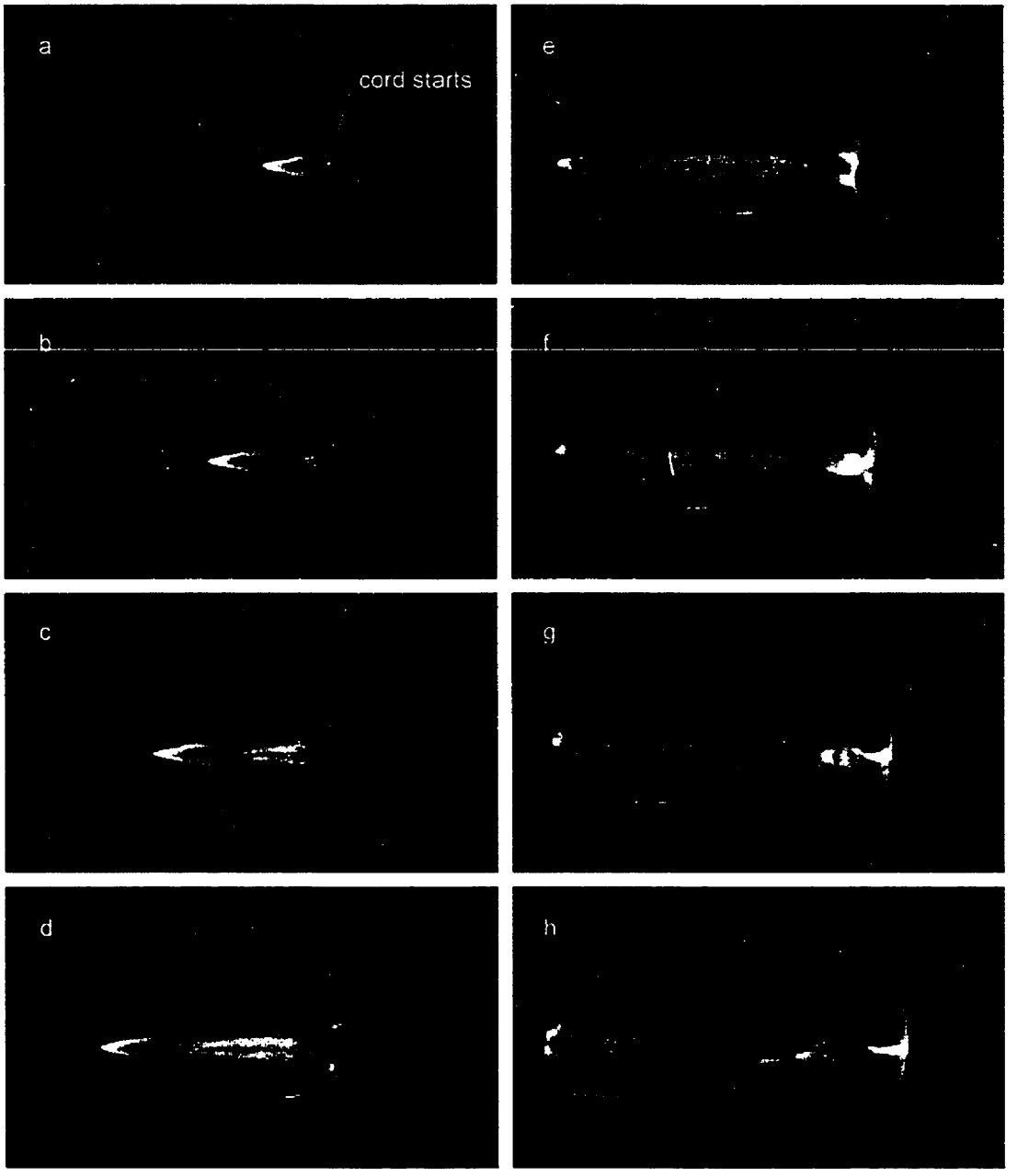

Fig. 4.8 Effect of finite length of detonating cord on the back field (Shot 53, $\phi = 1.08$, $E_S = 65$ kJ/m), frames taken 143 μsec apart

As the critical conditions for initiation are approached (i.e., by decreasing the fuel equivalence ratio for a given strength of cord), the flowfields become more complex. In Fig. 4.9, a photographic record for $\phi = 0.82$, $E_S = 260$ kJ/m is shown. The detonating cord initiated an oblique conical detonation. However,

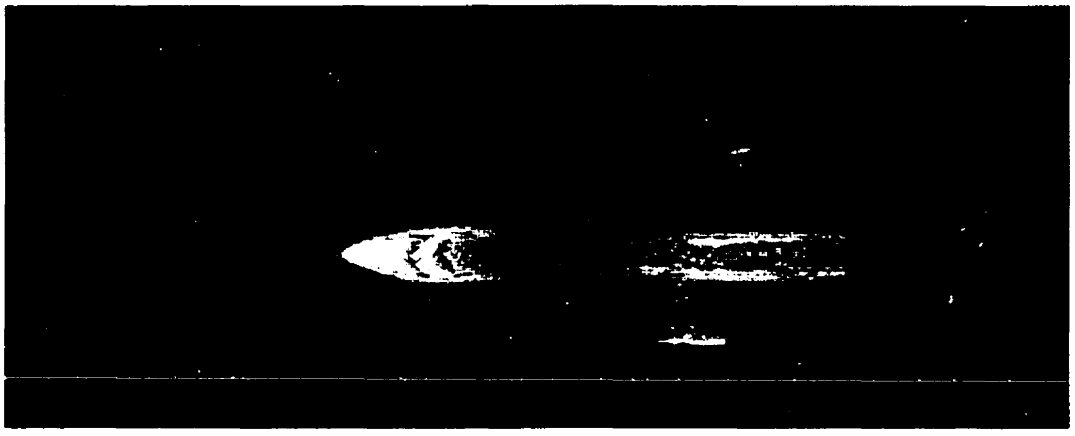

Fig. 4.9 Limit of the supercritical regime in C_2H_4 – Air (Shot 35, $\phi = 0.82$, $E_S = 260$ kJ/m)

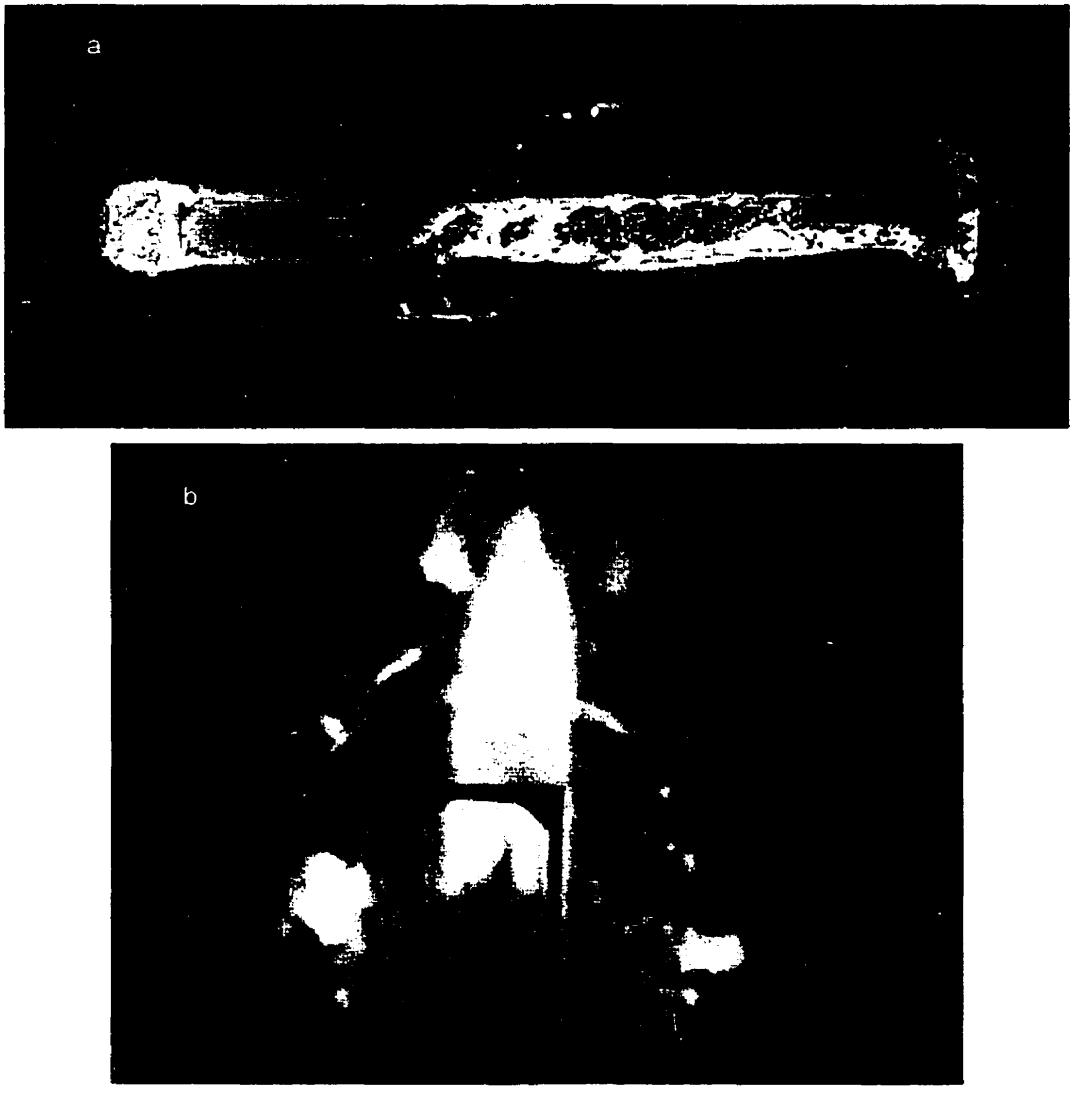

Fig 4.10 Critical regime in C_2H_4 – Air (Shot 47, $\phi = 0.7$, $E_S = 520$ kJ/m), a) side view, b) top view

the front of the detonation wave was more irregular and "indented" than for more sensitive mixtures (c.f., Fig. 4.5, $\phi = 0.94$, $E_S = 260$ kJ/m). It can be speculated that although the energy of the source was sufficient to create the critical states for the direct inititiation of detonation, local fluctuations in the mixture or cord strength could have retarded or advanced the onset of detonation. The initiation events became more stochastic, as three-dimensional effects of the initiation phenomena begin to play a role. The second feature that can be noticed from the photographic records of experiments approaching the critical regime is the quenching of the teardrop detonation in the back, caused by diffraction at the end of the cord. These expansions quenched the detonation wave in the back, which became no longer visible on the records. However, re-initiations subsequent to the diffraction appeared under the form of localized luminous hot spots. This clearly demonstrates that the energy of the source per unit length is approaching the critical value, since any attenuating effects (e.g. diffraction) may quench a critically initiated wave.

4.4.3 The Critical Regime of Initiation

When the mixture composition becomes critical, phenomena of increased complexity were observed. The blast wave no longer decayed monotonically to a conical Chapman Jouguet detonation wave. Instead, initiation was governed by the appearance of explosion centers within the shocked gas layer. Detonation "bubbles" developed from these localized explosion centers in the appropriate chronological sequence to coalesce and form an irregular conical detonation wave. This behavior was observed over the entire range of detonating cords investigated. Photographic evidence of this phenomena is shown in Fig 4.10 and 4.11 for $E_S = 520$ kJ/m, $\phi = 0.7$, and $E_S = 65$ kJ/m, $\phi = 1.03$, respectively. The detonation bubbles originated from a region close to the high explosive products, within the shocked gas layer. The second conclusion that is obtained from these records is that these detonation bubbles grew in a preferred direction, namely in the direction of propagation of the cord. This can be seen from the greater intensity of luminosity of the bubble in this direction (left hand side of the bubble in the photographs).

Near the limit of the critical regime, by further reducing the fuel equivalence ratio, a small number of explosion centers were sometimes observed to develop into local self-sustained spherical detonation bubbles, as can be seen in the successive frames of Figs. 4.12 and 4.13 (E_S = 65 kJ/m, ϕ = 0.98). The density of these explosion centers was insufficient to merge into a conical detonation. Instead, as the detonation bubbles grew, a highly asymmetrical front was formed. In the regions affected by these explosion centers, the blast wave re-accelerated to the CJ velocity, while the rest of the blast wave decayed, similar to the subcritical case. Eventually, after the detonation in the cord exited the bag, the much slower gaseous detonation bubbles encountered the bag boundary and transitioned to a planar detonation covering the entire cross section of the bag. The resulting detonation front propagated down the bag in pre-shocked gas at velocities close to the CJ velocity of the mixture.

The small number of explosion centers that appear on the records shown in Figs. 4.12 and 4.13 permitted an unambiguous analysis of the successive frames. The first conclusion is that these explosion centers consistently appear in a region very close to the cord. Within the limited resolution of these experiments, it appears that the explosion centers appear before the high explosive products have reached their maximum expansion, approximately 20 cm away from the cord's axis. For this mixture the cell size is approximately 2.7 cm (c.f. Appendix 1), thus the onset of detonation occurs at a radius less than 8λ.

The preferred direction of formation of the detonation bubbles is clearly evidenced by these series of frames (Fig. 4.12). These detonation bubbles developed from localized hot spots within the shocked gas layer and grew within the shocked gas. Each individual bubble initially grew preferentially in the direction of the cord propagation. For reference, the shape of the shock wave in air is shown in frame *c* of Fig. 4.12. It can be seen that part of the explosion centers overtake the leading shock while and the other part propagates into shocked but unreacted mixture. The intersection of the decaying shock, and the fronts of the bubble propagating into fresh mixture and into the shocked mixture to the left clearly defines a triple shock interaction. On the photographs, it corresponds to a distinctive "kink" in the bubble shape. Analysis of these succes-

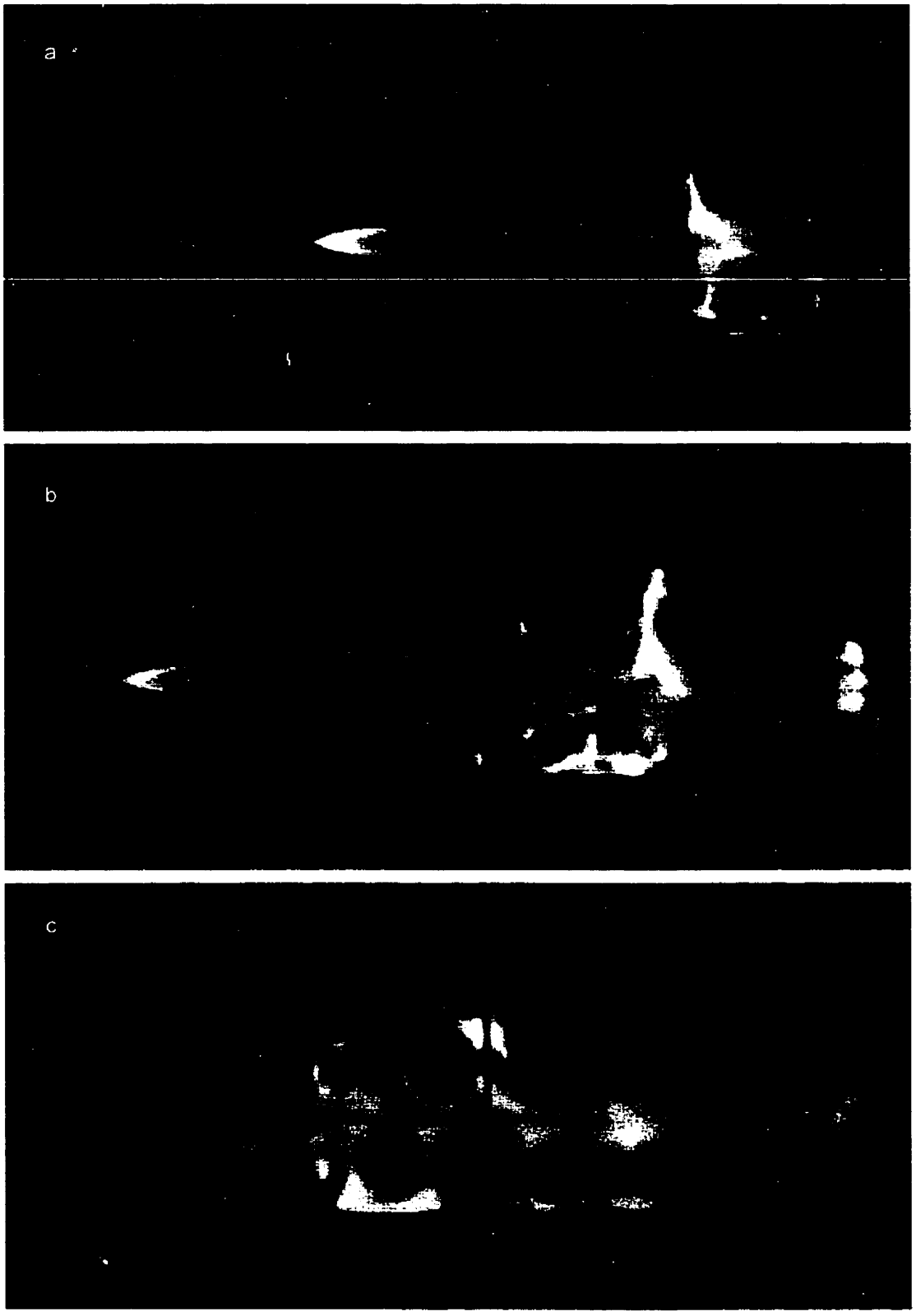

Fig. 4.11 Critical Regime in C_2H_4 – Air (Shot 44, $\phi = 1.03$, $E_S = 65$ kJ/m), 286 μsec between frames

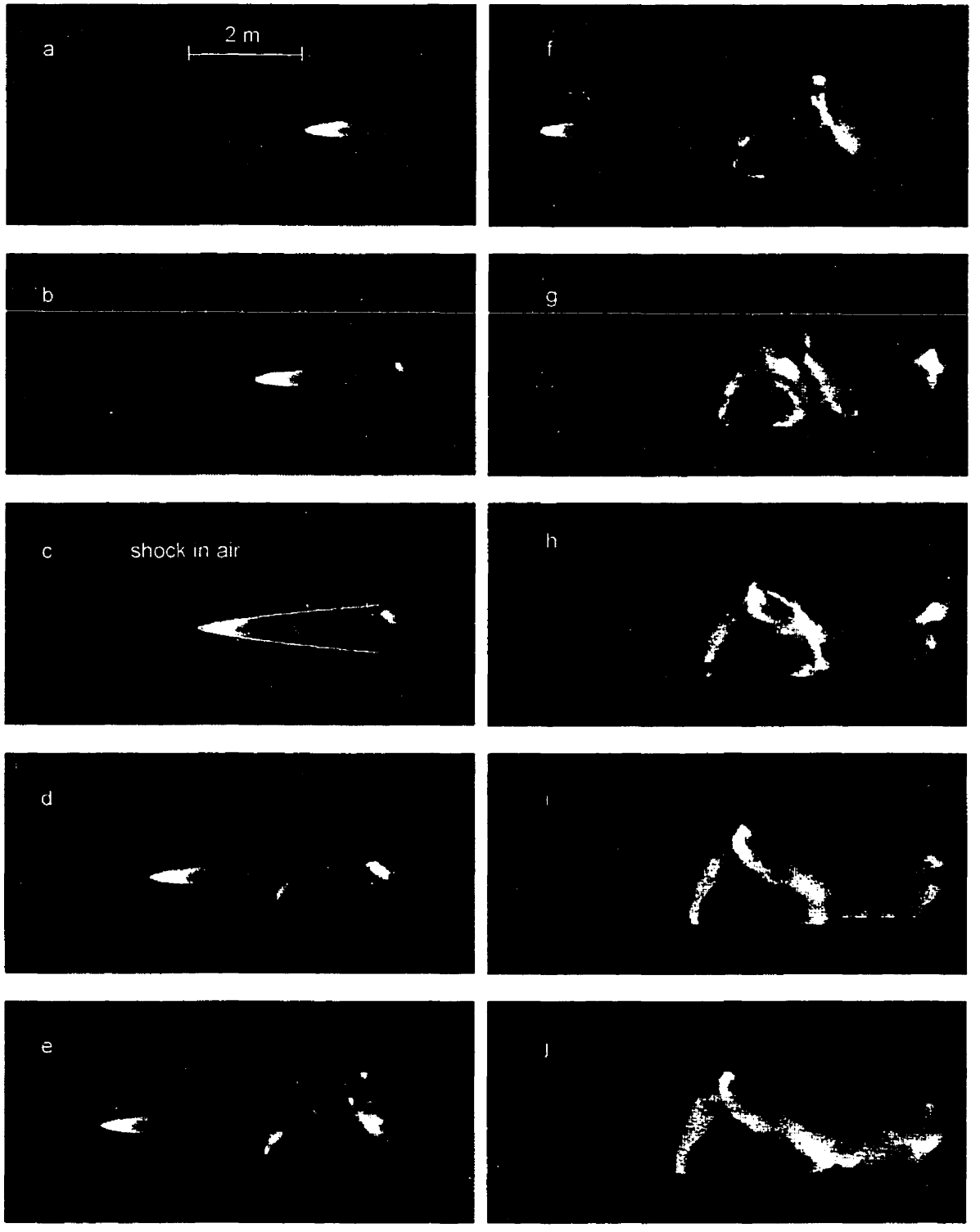

Fig. 4.12 Limit of the critical regime in C_2H_4 – Air
(Shot 42, ϕ=0.98, E_S = 65 kJ/m), frames 143 µsec apart

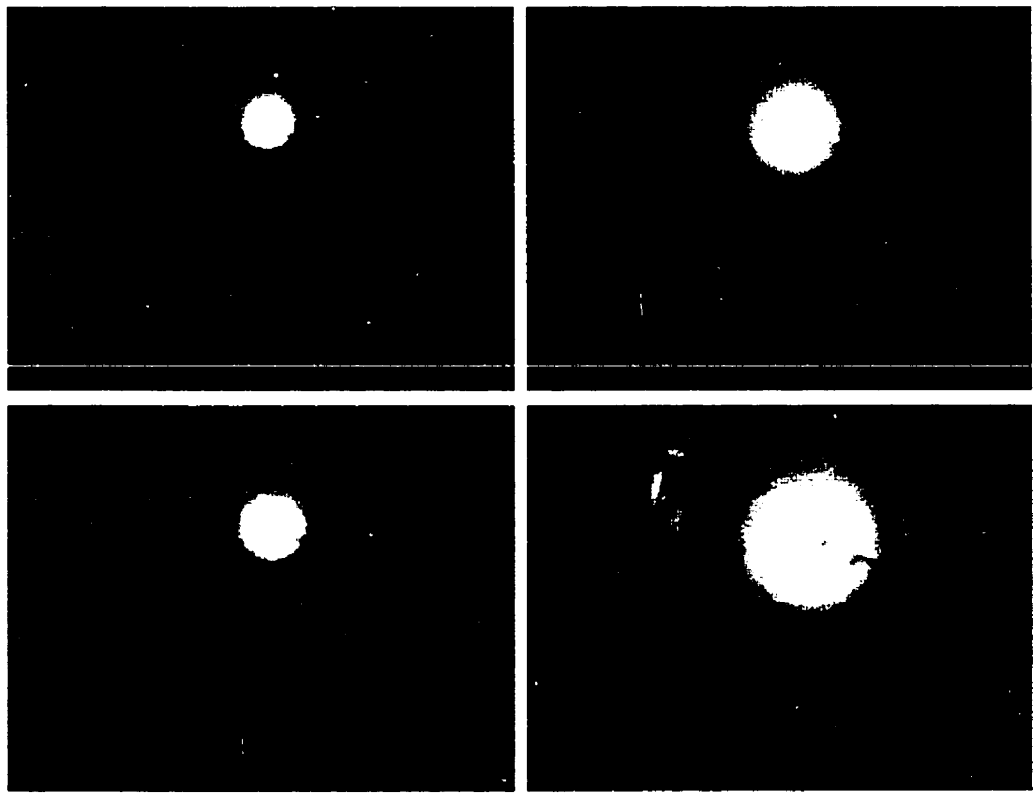

Fig. 4.13 Limit of the critical regime in C_2H_4 – Air
(same experiment as Fig. 4.12, head-on view)

-sive frames suggests that the triple shock configuration propagates into the shocked gas at the Chapman-Jouguet velocity of the mixture. This is similar to the critical regime previously observed in the spherical geometry. Abrupt localized explosion centers or "hot spots" appear between the initial shock and reaction front, and quickly grow to encompass the shocked but yet unreacted gas, as shown by the classic schlieren pictures taken by Knystautas (Bach et al., 1969), shown in Fig. 1.1.

4.5 Discussion of Results

The results of all the large scale experiments are summarized in Fig. 4.14. Each experiment is categorized as "subcritical", "critical", or "supercritical" as described above. Clearly, the data obtained separates the source energy-equivalence ratio ($E_S - \phi$) plane for lean ethylene-air mixtures in two separate regions, "Go" and "NoGo". For a given strength of cord, a decrease in the fuel

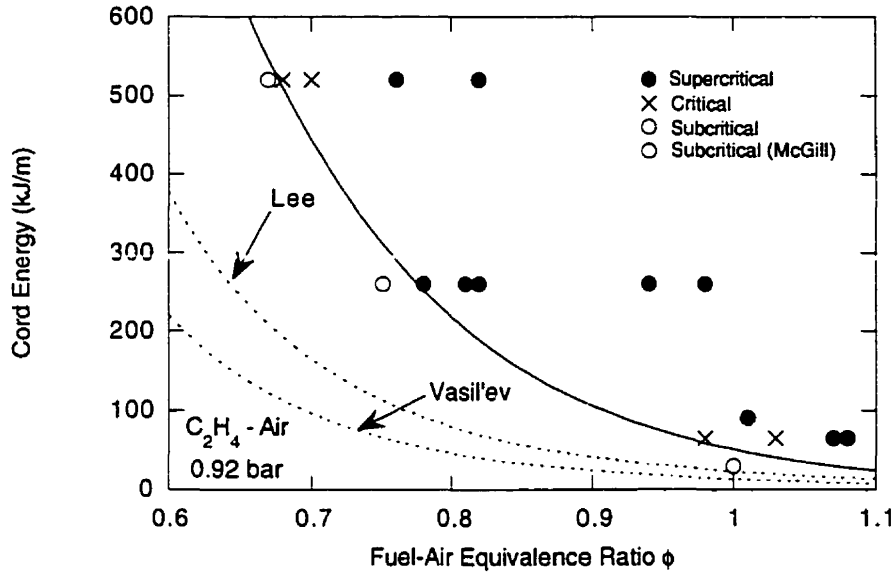

Fig. 4.14 Summary of experimental results and comparison with theory

equivalence ratio implies a decrease in the sensitivity of the mixture. Eventually, there exists a critical fuel-air equivalence ratio below which detonation is no longer initiated. The results can be summarized as follows, where ϕ^* denotes the critical fuel-air equivalence ratio below which no detonation is observed for a given detonating cord strength:

- *Supercritical regime*

  For $\phi >> \phi^*$, a conical teardrop shape detonation is directly initiated by the detonating cord.

  For $\phi > \phi^*$, a conical detonation is initiated; however, any attenuating effect (e.g., diffraction) may cause localized quenching.

- *Critical regime*

  For $\phi \approx \phi^*$ (i.e. $E_S \approx E_S^*$), stochastic localized detonations form within less than 8λ from the cord and further propagate in the surrounding shocked gas. The number of these localized spherical detonations governs the regularity of the resulting front.

- *Subcritical regime*

  When $\phi < \phi^*$ (i.e. $E_S < E_S$), detonation fails to initiate altogether, and the shock decays to low velocities, similar to a shock in inert gas (air).

The sensitivity of the mixture is reflected by the mixture cell size λ. The cell size of the ethylene-air mixtures has been studied extensively for wide ranges of initial conditions (Knystautas *et al.*, 1984, Murray *et al.*, 1984, Moen *et al.*, 1982, 1984), and can be correlated to the air-fuel equivalence ratio of the mixture (see Appendix A for the cell size of C_2H_4-Air mixtures). Reducing the fuel-air equivalence ratio results in an increased chemical induction period, thus an increase of the detonation cell width. Over the range of equivalence ratios investigated in this study (i.e. 0.67 – 1.08), for an initial pressure of 0.9 – 1.0 bar, the published data can be correlated well with a power law fit, yielding:

$$\lambda(\text{mm}) = 25.34\phi^{-2.9775} \qquad 4.2$$

Using this relationship, the experimental results can be presented on the $E_S - \lambda$ plane, as shown in Fig. 4.15. For purely cylindrical initiation, dimensional

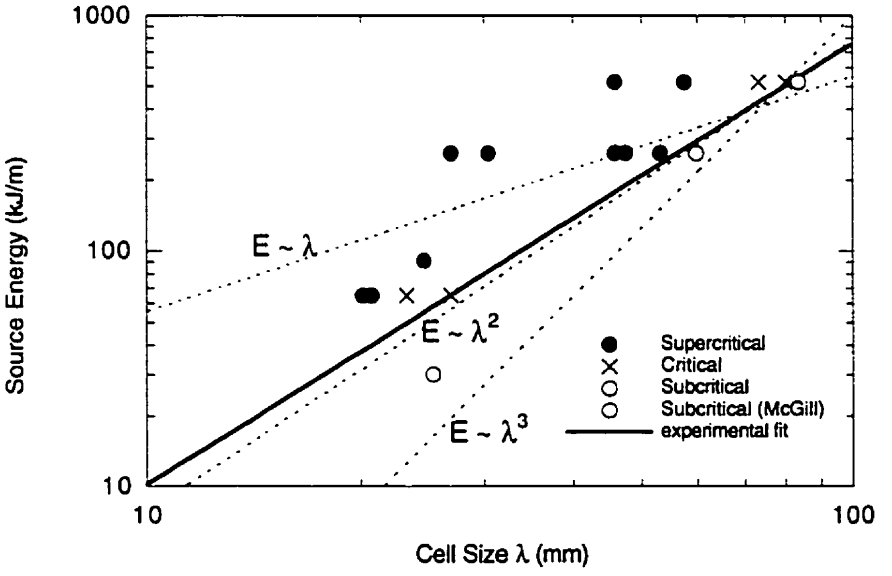

Fig. 4.15 Dependence of critical energy on λ^2 for the cylindrical geometry

arguments require that the critical energy of the source scales with the square of the cell size. From our experiments, on a log-log plot, the slope of the line delimitating "Go" and "NoGo" conditions for initiation is approximately 2 (i.e. $E_S^* \propto \lambda^2$). For comparison, lines with slopes of 1 and 3 are also shown, corresponding with critical initiation of planar ($E_S^* \propto \lambda$) and spherical detonations ($E_S^* \propto \lambda^3$), respectively. The planar and spherical cell dependencies clearly disagree with the experimental data. Thus, the critical energy dependence on λ^2 provides substantial evidence for the cylindrical nature of the flowfield driven by the detonating cord.

In Fig. 4.14, the experimentally determined critical conditions are compared with cylindrical initiation theory. The estimates for critical energy to initiate a cylindrical detonation given by Lee (Eq. 3.3) and Vasil'ev (Eq. 3.5) are shown as a function of fuel-air equivalence ratio. Both theoretical estimates clearly underestimate by a factor of 2 – 3 the critical energy found experimentally.

Chapter 5 Geometry Scaling of Direct Initiation

The dependence of critical energy on the square of the cell size, as shown in the previous chapter, suggests that the detonating cord experiments are close to the ideal limit of a purely cylindrical geometry. In view of the discrepancies between the initiation models of Lee and Vasil'ev for a cylindrical detonation and the present experiments, it appears worthwhile to re-assess the important length scales and parameters that are involved in purely cylindrical detonations, and show how these values are linked with the critical parameters for other geometries (e.g., spherical, planar).

The trajectory of a reacting blast wave before the onset of detonation can be approximated by the classic similarity solution for non-reacting strong blast waves, where at any instant of time the shock radius R_S, the strength of the shock M_S and the source energy E_S are related by

$$E_S = \alpha_j \left(\frac{j+2}{2} \right)^2 \gamma P_o M_S^2 R_S^j \qquad 5.1$$

where α_j is a constant obtained from blast wave theory ($\alpha_1 = 1.009$, $\alpha_2 = 0.986$, $\alpha_3 = 0.851$, for $\gamma = 1.4$) which depends weakly on the adiabatic exponent γ, P_o is the initial mixture pressure and the index j represents the geometry of the wave (i.e., j = 1, 2, 3 for planar, cylindrical and spherical geometries, respectively) (Sedov, 1959).

Following Zeldovich's criterion (Zeldovich *et al.*, 1956), the critical source energy required to directly initiate a detonation should be such that a blast wave above a critical strength (M_S*) is maintained over a critical distance of travel (R_S*). Thus, from Zeldovich's criterion, the determination of the critical energy E_S* necessitates two parameters to be specified, M_S* and R_S*.

The critical Mach number inferred by velocity profiles obtained in Chapter 3, i.e., the minimum shock strength prior to the onset of detonation, is clearly between M_{CJ} and $0.5M_{CJ}$. The correct choice of M_S* should reflect the critical shock strength below which any detonation would fail. Thus, the lower

bound, which corresponds to the auto-ignition limit is the appropriate value ($M_S^* \approx 0.5M_{CJ}$), which corresponds to the value chosen by Lee (1997).

The choice of the critical radius R_S^* at which the onset of detonation occurs is a more difficult task. It is usually correlated to some characteristic length scale of the detonation, usually the cell width λ or cell length l ($l \approx 1.6\lambda$). For the initiation of spherical detonations, the experiments of Elsworth *et al.*. (1984) in ethane-oxygen-nitrogen suggest that the critical radius at which the first explosion bubbles are observed is approximately 10λ. This conclusion is obtained from measurements of the combustion velocity profile using microwave interferometry and flow visualization. A typical streak photograph (equivalent to an r - t diagram) is shown in Fig. 5.1. The resemblance to the present experiments is striking: after a critical distance R_S^* of approximately 10λ, sudden explosion bubbles appear. Similarly, Bull *et al.* (1978) measured the critical "kernel" distance in stoichiometric ethylene-air mixtures. From microwave interferometry measurements of the combustion front, they deduce a critical radius of 0.232m. Since the cell width of stoichiometric ethylene-air at atmospheric conditions is approximately 2.3 cm (c.f Appendix A), the critical radius is again approximately 10λ. Thus, the critical conditions for initiation of spherical hydrocarbon-air gaseous detonations occur at critical radius of $R^*_{spherical} \approx 10\lambda$.

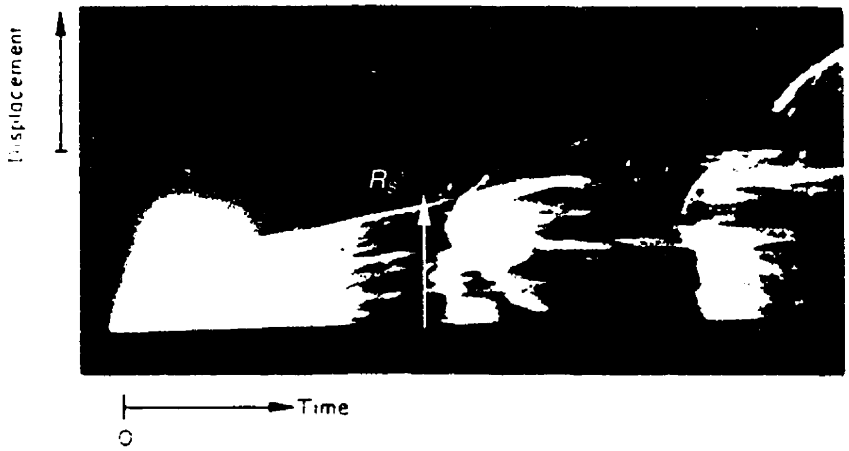

Fig. 5.1 Streak photograph of a critically initiated spherical detonation in $2.3C_2H_6 + 3.5O_2 + 3.5N_2$ (taken from Elsworth *et al.*, 1984)

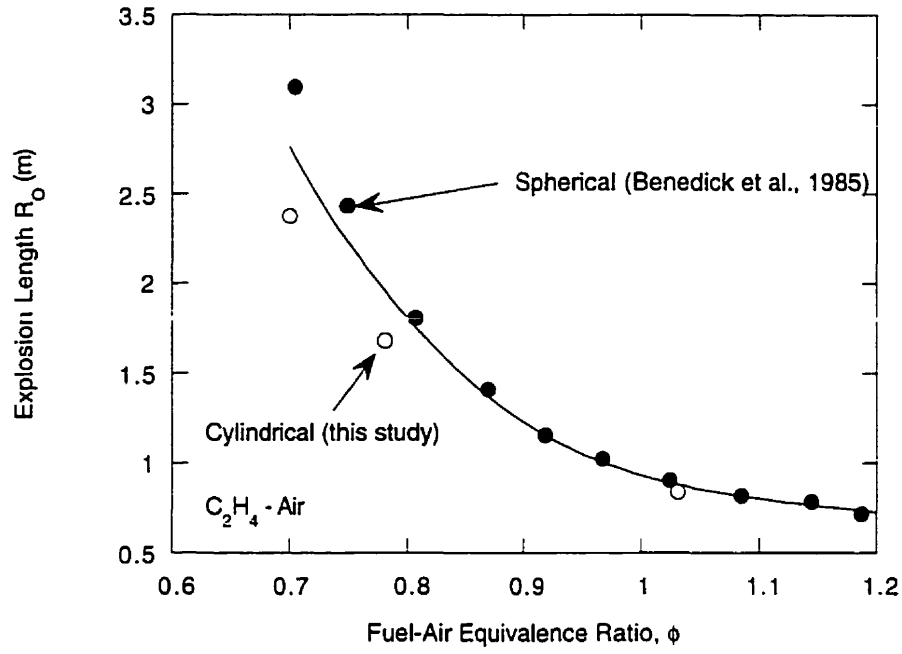

Fig. 5.2 Invariance of explosion length in the cylindrical and spherical geometries

For the cylindrical geometry, one would expect a different value for the critical radius, since the curvature of the wave is different. The link between the different values of critical radii R_s*'s for the different geometries is the explosion length $R_o \equiv (E/P_o)^{1/j}$, where j is the geometric index. The explosion length is the only length scale associated with strong blast decay, since it represents a scaling length for the source energy of a spherical, cylindrical and planar blast. For critical direct initiation of detonation, experiments indicate that the critical explosion length is invariant with geometry, as suggested by Lee (1977). The invariance between the critical explosion length in cylindrical and spherical geometries is verified in Fig. 5.2, where the present experiments in ethylene-air are compared with the experiments of Elsworth, reported in Benedick *et al.* (1985), for the same mixture in the spherical geometry. It can be seen that the explosion length is invariant between the spherical and cylindrical geometries.

The explosion length scaling is of prime importance, as it permits linking the critical initiation energy, energy per unit length and energy per unit area for the three basic geometries.

$$R_o \equiv \left(E_j / P_o\right)^{\frac{1}{j}} \approx \text{const} \qquad 5.2$$

$$\frac{E_{spherical}}{E_{cylindrical}} \approx \frac{E_{cylindrical}}{E_{planar}} \approx R_o \qquad 5.3$$

Consequently, if the critical energy is known in one geometry, it can simply be deduced for another geometry. Furthermore, such simple energetic scaling permits us to obtain a scaling relationship between the critical radii R^*_{planar}, $R^*_{cylindrical}$ and $R^*_{spherical}$. Substititing Eq. 5.1 in the scaling law (Eq. 5.3), for $\gamma = 1.4$ and $M_s^* \approx 0.5 M_{CJ} \approx 2.8$ (i.e. where M_{CJ} was taken as 5.5, typical of hydrocarbon–air mixtures), we get

$$R^*_{cylindrical} \approx 0.59\, R^*_{spherical} \approx 0.59(10\lambda) \approx 5.9\lambda \qquad 5.4$$

$$R^*_{planar} \approx 0.16\, R^*_{spherical} \approx 1.6\lambda \qquad 5.5$$

These scaling laws are shown graphically in Fig. 5.3, where the blast wave Mach number prior to the onset of detonation is plotted versus increasing radial distance normalized by explosion length R_o, for planar, cylindrical, and spherical blasts. The fact that the critical radius decreases as geometry goes from spherical to cylindrical to planar can simply be explained by invoking the critical curvature concept: a cylindrical wave has less curvature than a spherical one for the same radius so it is able to initiate a self-sustained detonation closer to the source. Perhaps the most fundamental conclusion is that the critical radius to initiate a planar detonation wave is approximately one cell length (~1.6λ), which represents the smallest possible critical radius when the wave is not subject to any curvature effect, and only unsteadiness can cause wave quenching.

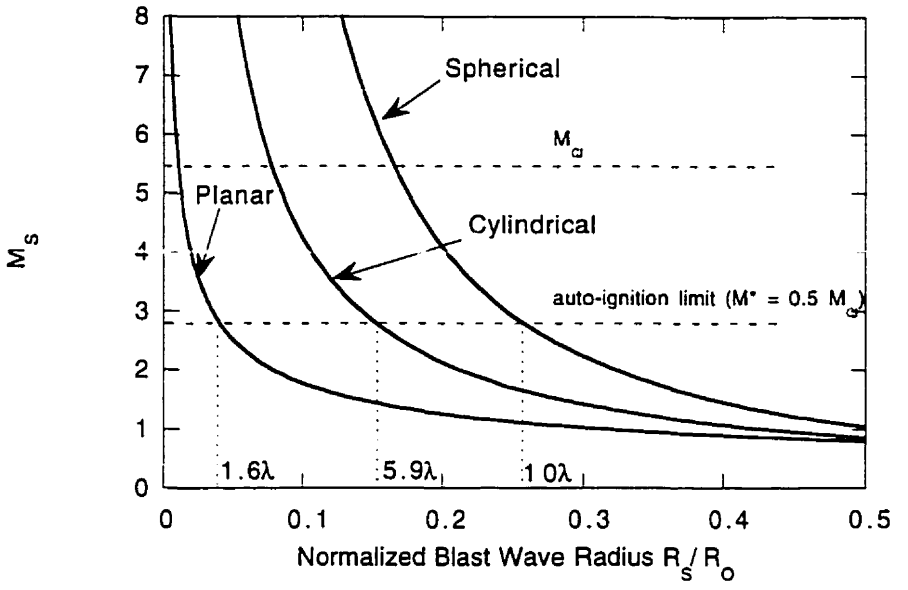

Fig. 5.3 Critical radius scaling between geometries

The critical radius of 5.9λ for the cylindrical geometry is in good agreement with the present study. In Chapter 3, it was shown that large fluctuations in the velocity profiles of the combustion front, typical of explosion centers, occurred consistently at a distance of 4 to 6λ from the detonating cord (c.f. Table 3.1, Chapter 3). Similarly, the photographic evidence presented in Chapter 4 showed that the ignition centers in the critical regime were observed at distances less than 8λ away from the cord.

For the planar case, the scaling relationship for the critical radius (Eq. 5.5) remains to be verified. However, the study of Benedick (1979) on stoichiometric methane-air mixtures initiated by planar sheets of high explosive indicates that the critical radius in this geometry for this mixture is less than 1 m. The cell size λ of this mixture is approximately 35 cm (Beeson *et al.*, 1991), yielding a critical radius less than 3λ, in good accord with the present prediction based on geometry scaling (Eq. 5.5).

Next we turn to the critical energy estimation. Substituting the values of critical radii and shock strength in the expression for critical energy (Eq. 5.1), we

find the following relationships for critical energy, which are tabulated along with the other critical parameters in Table 5.1.

Table 5.1 Critical parameters for direct initiation of planar, cylindrical and spherical detonations

	Spherical	*Cylindrical*	*Planar*
j	3	2	1
R_s^*	10λ	5.9λ	1.6λ
M_s^*	$0.5\,M_{CJ}$	$0.5\,M_{CJ}$	$0.5\,M_{CJ}$
E_s^*	$1330\gamma P_o M_{CJ}^2 \lambda^3$	$34.3\gamma P_o M_{CJ}^2 \lambda^2$	$0.91\gamma P_o M_{CJ}^2 \lambda$

The critical energy estimate for the spherical geometry correlates very well with the experimentally determined values of Elsworth (Benedick *et al.*, 1985) for ethylene-air mixtures at atmospheric conditions (Fig. 5.4). For the planar case, it is very difficult to compare with experiment, since conclusive data do not exist in the literature. For the cylindrical geometry, the estimate for the critical energy is compared with the present experimental results in Fig. 5.5 for

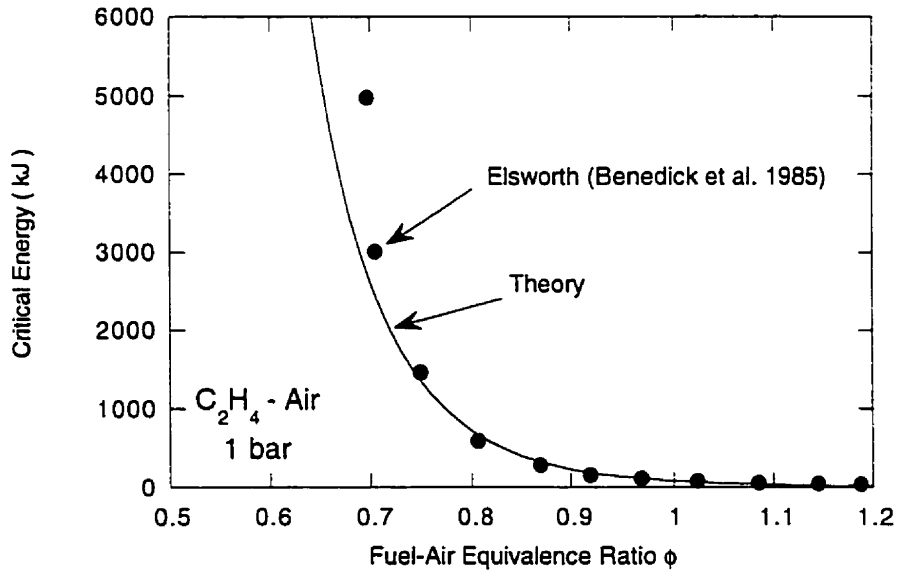

Fig. 5.4 Comparison between critical energy results of Elsworth (Benedick *et al.*, 1985) in C_2H_4 – Air mixtures in the spherical geometry and theory

the results obtained in the large-scale experiments in ethylene-air (c.f. Chapter 4). It can be seen that the theoretical estimate agrees very well with the present data. The good agreement between the scaling laws and the experimental data in both the spherical and cylindrical geometries clarifies the correct length scales that should be used in the theory of direct initiation of detonations.

As mentioned in the Introduction, previous experiments in the cylindrical geometry presented significant non-idealities, mainly because the cylindrical geometry was simulated by having a thin, confined cylindrical slice. The most recent and extensive study is that of Aminallah *et al.* (1993). It is thus worthwhile comparing their critical energy results in methane–oxygen mixtures with the present estimate of critical energy. Due to the non-idealities of their experimental set-up, the critical energy for a given mixture composition required extrapolation to infinite chamber width, thus introducing some uncertainties in their measures. Their experimental results are shown in Fig. 5.6 along with the present estimate of critical energy. The cell data for methane-oxygen mixtures is taken from Aminallah *et al.* (1993), Manzhalei *et al.* (1974), and Bauer *et al.* (1985) (c.f. Appendix A). Adequate agreement for the critical energy is found with the

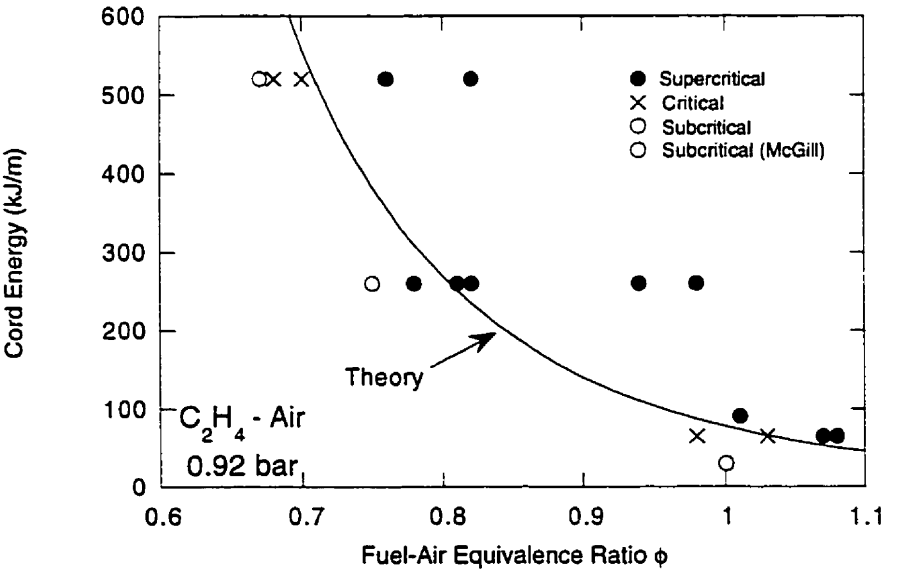

Fig. 5.5 Comparison between present results in C_2H_4 – Air and theory

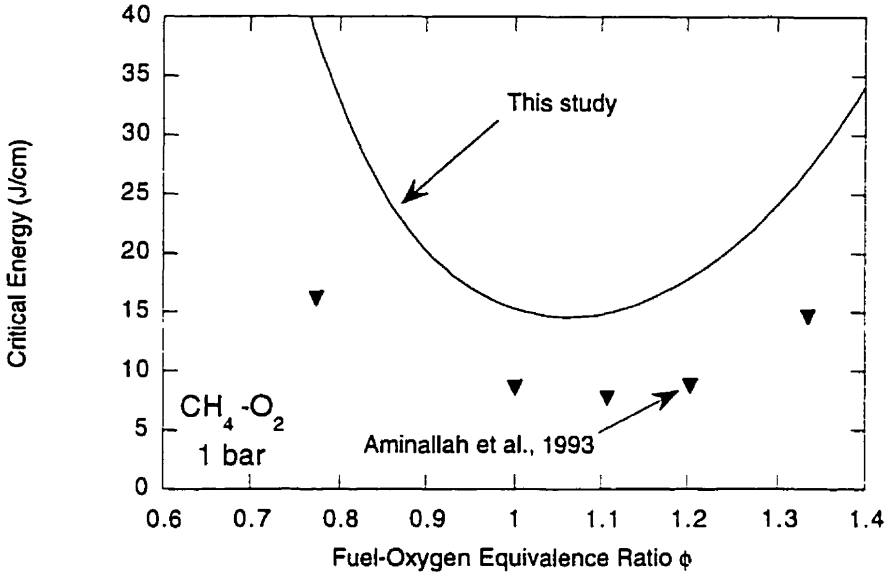

Fig. 5.6 Comparison between critical energy measured by Aminallah *et al.* (1993) in $CH_4 - O_2$ and the present experiments

present study, considering the wide scatter in the cell size data for this mixture (c.f. Appendix A). Although good agreement is found between Aminallah's critical energy measurements and the present study, these authors reported a pre-detonation radius of 20λ (Sochet, Aminallah, and Brossard, 1997), which is in significant discord with the values of critical radius found in the present study (4 - 8λ). It is suspected that Aminallah's observations of the critical radius in the cylindrical geometry are highly influenced by the confined nature of their experiments. It is well known that wall effects and confinement can cause flame acceleration to detonation (DDT) in mixtures that are not directly initiated by the source. Such initiation would be observed at larger radii than in direct initiation. This behavior can also explain why their critical energy is smaller by a factor of two than the one found in the unconfined experiments of the present study.

Chapter 6 Conclusions

This study showed that the direct initiation of cylindrical detonations can be investigated with the detonating cord technique in the limit of the cylindrical geometry. This technique eliminated the confinement effects present in previous studies and permitted an unambiguous analysis of the flowfields corresponding to each regime of initiation.

The flow field established by the detonating cord resembles that of a hypersonic projectile. The expanding high explosive detonating cord products, which act as an impermeable piston, drive a strong bow shock into the surrounding gas. Since the detonation velocity in the cord is very high (6 – 7 km/s), beyond the immediate vicinity of the cord the flow field can accurately be analyzed using the hypersonic small disturbance theory for slender projectiles. It was shown that the blast wave analogy was adequate to model the flow field, where a series of cylindrically expanding blast waves are successively synchronized by the detonation velocity in the cord. The results obtained from experiments performed in inert gas were similar to the subcritical case of initiation in combustible gas. In both cases, the blast wave decays to an acoustic wave. Beyond the vicinity of the cord, the trajectory of the decaying blast wave agrees well with cylindrical blast wave theory for inert gas.

In the supercritical regime of initiation, where the strength of the cord exceeds the critical energy per unit length to initiate a cylindrical detonation, the blast wave driven by the detonating cord decays monotonically to a stable CJ detonation wave. Due to the finite velocity in the cord, the resulting detonation wave is a conical one. Based on photographic evidence and measurements of the velocity of the detonation, it was shown that the oblique detonation is self-sustained and stable. The wave angle agrees with theoretical considerations. The long debated stability of oblique CJ detonations (Pratt *et al.*, 1991, Shepherd, 1994) was finally confirmed. This result has significance for applications that seek to exploit stabilized detonation waves for propulsive purposes.

In the critical regime of initiation, it was shown that the onset of detonation is always via the development of localized explosion centers. These

detonation kernels grow within the shocked gas layer at velocities close to the CJ velocities and merge to form an asymmetrical detonation front. A similar mechanism was previously observed in the critical regime of initiation for spherical detonations (Bach *et al.*, 1969). This suggests that the mechanism of initiation is similar for all geometries.

The critical shock radius at which the onset of detonation occurs in the critical regime was correlated to the detonation cell size of the mixtures investigated, yielding $4 - 8\lambda$ throughout the experiments. Using the invariance of the explosion length R_o in the critical regime of initiation of spherical, cylindrical and planar detonations, it was shown how the critical radii and critical energies scale between the different geometries. The good agreement between the different scaling laws and our experimental results clarifies the correct length scales that should be used in the theory of direct initiation of detonation.

References

Aminallah, M., Brossard, J. & Vasil'ev A. 1993 Cylindrical detonations in methane-oxygen-nitrogen mixtures, *Prog. Astro. Aero.*, 153:203-228.

Bach, G.G. & Lee. J.H. 1969 Higher-order perturbation solutions for blast waves. *AIAA J.*, 7:742-744.

Bach, G.G., Knystautas, R. & Lee J.H. 1969 Direct Initiation of spherical detonation in gaseous explosives, *12th Symp. (Int.) Comb.*, The Combustion Institute, Pittsburgh, PA, 853-864.

Bauer, P., Presles, H.N., Heuze, O. & Brochet, C. 1986 Measurement of cell lengths in the detonation front of hydrocarbon oxygen and nitrogen mixtures at elevated initial pressures, *Comb. Flame*, 64(1):113-123.

Bauer, P., 1985 Contribution à l'étude de la détonation des mélanges explosifs gazeux à pression initiale élevée, PhD thesis, Université de Poitiers.

Beeson, H.D., McClenagan, R.D., Bishop, C.V., Benz. F.J., Pitz, W.J., Westbrook, C.K. & Lee, J.H.S. 1991 Detonability of hydrocabon fuels in air, *Prog. Astro. Aero.*, 133:19-36.

Behrens, H., Struth, W. & Wecken, F. 1965 Studies of hypervelocity firings into mixtures of hydrogen with air or with oxygen, *10th Symp. (Int.) Comb.*, The Combustion Institute, Pittsburgh, 245-252.

Benedick, W.B, Guirao, C., Knystautas, R. & Lee, J.H. 1985 Critical charge for the direct initiation of detonation in gaseous fuel-air mixtures, *Prog. Astro. Aero.*, 106:181-202.

Benedick, W.B. 1979 High-explosive initiation of methane-air detonations, *Comb. Flame*, 35:87-91.

Brode, H.L. 1959 Blast wave from a spherical charge, *Phys. Fluids*, 2:217-229.

Bull, D.C., Elsworth, J.E. & Hooper, G. 1978 Initiation of spherical detonation in hydrocarbon/air mixtures, *Acta Astro.*, 5:997-1008.

Chernyi, G.G. 1961 *Introduction to hypersonic flow*, Academic Press, New York.

Chue, R.H.S. 1993 High speed deflagration and its transition to detonation, PhD. Thesis, McGill University, Canada.

Dobratz, B.M. & Crawford, P.C. 1985 LLNL Explosives handbook , UCRL-52997, Livermore, CA: Lawrence Livermore National Laboratory.

Edwards, D.H., Hooper, G., Morgan, J.M. & Thomas, G.O. 1978 The quasi-steady regime in critically initiated detonation waves, *J. Phys. D.: Appl. Phys.*, 11:2103-2117.

Elsworth, J.E., Shuff, P.J. & Ungut, A. 1984 "Galloping" gas detonations in the spherical mode, *Prog. Astro. Aero.*, 94:130-150.

Endo, T., Kasahara, J., Takeishi, A. & Fujiwara, T. 1997 Experiments on oblique detonation waves around hypersonic cone-nosed projectiles, *Conference Proceedings, 16th International Colloquium on the Dynamics of Explosions and Reactive Systems*, Cracow, Poland, 473-476.

Fried, L.E. 1996 *Cheetah v.* 1.4, Energetic Material Center, Lawrence Livermore National Laboratory.

Fry, R.S. & Nicholls, J.A. 1969 Blast wave initiation of gaseous and heterogeneous cylindrical detonations, 12th *Symp. (Int.) Comb.*, The Combustion Institute, Pittsburgh, 43-52.

Funk, J.W. & Murray, S.B. 1982 The DRES large-scale fuel-air explosives testing facility, Memorandum SM-1051, Defence Research Establishment Suffield, Ralston, Alberta, Canada.

Guirao, C.H., Knystautas, R., Lee, J., Benedick, W. & Berman, M. 1982 Hydrogen-air detonations, *19th Symp. (Int.) Comb.*, The Combustion Institute, Pittsburgh, 583-590.

Hayes, W.D. & Probstein, R.F. 1966 *Hypersonic Flow Theory, Vol. 1, Inviscid Flows*, Academic Press, New York.

Hertzberg, A., Bruckner, A.P. & Bogdanoff, D.W. 1988 Ram accelerator: a new chemical method for accelerating projectiles to ultrahigh velocities, *AIAA J.*, 26:195-203.

Higgins, A.J. & Bruckner, A.P. 1996 Experimental investigation of detonation initiation by hypervelocity blunt projectiles, AIAA Paper 96-0342, 34th AIAA Aerospace Sciences meeting, Reno, NV.

Kaneshige, M. & Shepherd, J.E. 1997 Detonation Database, Explosion Dynamics Laboratory Report FM97-8, Graduate Aeronautical Laboratories California Institute of Technology.

Kaneshige, M.J. & Shepherd J.E., 1996 Oblique detonation stabilized on a hypervelocity projectile, *26th Symp. (Int.) Comb.*, The Combustion Institute, Pittsburgh, 3015-3022.

Knystautas, R., Guirao, C., Lee, J.H. & Sulmistras, A. 1984 Measurement of cell size in hydrocarbon-air mixtures , and predictions of critical tube diameter, critical initiation energy, and detonability limits, *Prog. Astro. Aero.*, 94:23-37.

Knystautas, R., Lee, J.H. & Guirao, C.M. 1982 The critical tube diameter for detonation failure in hydrocarbon-air mixtures, *Comb. Flame*, 48(1):63-83.

Lee, J.H. 1984 Dynamic parameters of gaseous detonations, *Ann. Rev. Fluid. Mech.*, 16:311-336.

Lee, J.H., Knystautas, R. & Bach, G.G. 1969 Theory of Explosions, MERL Report No. 69-70, McGill University, Montreal.

Lee, J.H.S. & Moen, I.O. 1980 The mechanism of transition from deflagration to detonation in vapor cloud explosions, *Prog. Energy Combust. Soc.* 6:358-389.

Lee, J.H.S. 1965 The propagation of shocks and blast waves in a detonating gas, Ph.D. Thesis, McGill University, Canada.

Lee, J.H.S. 1977 Initiation of gaseous detonation, *Ann. Rev. Phys. Chem.*, 28:75-104.

Lee, J.H.S. 1997 Initiation of detonation by a hypervelocity projectile, *Prog. Astro. Aero.* 173:293-310.

Lee, J.H.S. & Higgins, A.J. 1999 Comments on criteria for direct initiation of detonations, *Proc. Roy. Soc. A* (in press).

Lehr, H.F. 1972 Experiments on shock-induced combustion, *Astro. Acta*, 17:589-597.

Lin, S.C. 1954 Cylindrical shock waves produced by instantaneous energy release, *J. Applied Phys.*, 25(1):54-57.

Manzhalei, V.I., Mitrofanov, V.V. & Subbotin, V.A. 1974 Measurement of inhomogeneities of a detonation front in gas mixtures at elevated pressures, *Fiz. Goreniya Vzryva*, 10(1):89-95.

Matsui, H. & Lee, J.H. 1976 Influence of electrode geometry and spacing on the critical energy for direct initiation of spherical gaseous detonations, *Comb. Flame*, 27:217-220.

McVey, J.B. & Toong, T.Y. 1971 Mechanism of instabilities of exothermic hypersonic blunt-body flows, *Comb. Sci. Tech.*, 3:63-76.

Moen, I.O., Funk, J.W., Ward, S.A., Rude, G.M. & Thibault, P.A. 1984 Detonation length scales for fuel-air explosives, *Prog. Astro. Aero.*, 94:55-79.

Moen, I.O., Murray, S.B., Bjerketvedt, D., Rinnan, A., Knystautas, R. & Lee, J.H. 1982 Diffraction of detonation from tubes into a large fuel-air explosive cloud, *19th Symp. (Int.) Comb.*, The Combustion Institute, Pittsburgh, 635-644.

Murray, S.B. & Lee, J.H. 1984 The influence of yielding confinement on large-scale ethylene-air detonations, *Prog. Astro. Aero.*, 94:80-103.

Murray, S.B. 1984 The influence of initial and boundary conditions on gaseous detonation waves, Ph.D. Thesis, McGill University, Canada.

Nicholls, J.A., Sichel, M., Gabrijel, Z., Oza, R.D. & Vandermolen, R. 1978 Detonability of unconfined natural gas-air clouds, *17th Symp. (Int.) on Comb.*, The Combustion Institute, Pittsburgh, 1223-1234.

Pratt, D.T., Humphrey, J.W. & Glenn, D.E. 1991 Morphology of standing oblique detonation waves, *J. Propuls. Power*, 7(5):837-845.

Reynolds, W.C. 1981 STANJAN Chemical Equilibrium Solver, Stanford University.

Ruegg, F.W. & Dorsey, W.W. 1962 A missile technique for the study of detonation waves, *J. Res. Natl. Bur. Std. 66C*(1), 51-58.

Sakurai, A. 1953 On the propagation and structure of the blast wave Part I, *J. Phys. Soc. of Japan*, 8(5):662-669.

Sakurai, A. 1954 On the propagation and structure of the blast wave Part II, *J. Phys. Soc. of Japan*, 9(2):256-266.

Sedov, L.I. 1959 *Similarity and Dimensional Methods in Mechanics*, 4th ed., Academic Press, New York.

Sommers, W.P. & Morrison, R.B. 1962 Simulation of condensed explosive phenomena with gases, *Phys. Fluids*, 5:2:241-248.

Shepherd, J.E. & Lee, J.H.S. 1992 On the transition from deflagration to detonation, *Major Research Topics in Combustion*, 439-490.

Shepherd, J.E. 1994 Detonation waves and propulsion, *Combustion in High Speed Flows*, J. Buckmaster *et al.* (eds.), Kluwer Academic Publishers, 373-420.

Sichel, M. 1992 Transition to detonation, role of explosion within an explosion, *Major Reasearch Topics in Combustion*, 491-528.

Smeets, G. 1995 The ramaccelerator: perspectives and experimental results already achieved, IUTAM Symposium on Combustion in Supersonic Flows, Kluwer, Poitiers, October 1995.

Sochet, I., Aminallah, M. & Brossard, J. 1997 Detonability of fuel-oxygen and fuel-air mixtures, *Shock Waves*, 7(3):153-174.

Strehlow, R.A. 1969 The nature of transverse waves in detonations, *Astro. Acta*, 14(5):539-548.

Struth, W., Behrens, H. & Wecken, F. 1963 Untersuchung chemischer Reaktionen bei Einschuβ in reagierende gase oder Gasgemische mit hohen Geschwindigkeiten, *Technische Mitteilung ISL T9/63*.

Vasil'ev A.A. & Grigoriev V.V. 1980 Critical conditions for gas detonation in sharply expanding channels, *Fiz. Goreniya Vzryva*, 16(5):117-125.

Vasil'ev, A.A. & Nikolaev, Yu.A. 1978 Closed theoretical model of a detonation cell, *Acta Astro.*, 5:983-996.

Vasil'ev, A.A. 1983 Geometric limits of gas detonation propagation, *Fiz. Goreniya Vzryva*, 18(2):245-249.

Vasil'ev, A.A. 1997 Gaseous fuels and detonation hazards, 28th *International Conference of ICT*, June 1997, Karlsruhe, Germany.

Vasil'ev, A.A., Mitrofanov, V.V. & Topchiyan, M.E. 1987 Detonation waves in gases, *Fiz. Goreniya Vzryva*, 23(5):109-131.

Vasiljev, A.A. 1994 Initiation of gaseous detonation by high speed body, *Shock Waves*, 3:321-326.

Wecken, F. 1951 Memoire 14, Laboratoire de Recherche de St. Louis.

Zeldovich, Ya. B., Kogarko, S.M. & Simonov, N.N. 1957 An experimental investigation of spherical detonation in gases, *Soviet Physics-Technical Physics*, 1:1689-1713.

Appendix 1 Cell Sizes and CJ Parameters of the Mixtures Investigated

A1 Cell Sizes

Real detonation waves are characterized by a highly unsteady three-dimensional structure. The three dimensional structure can be observed by the "fish scale" patterns etched on the walls of detonation tubes which are evenly coated with smoke or soot prior to the experiment. These patterns result from the soot re-arrangement by the passage of the triple points in the detonation wave. A schematic of the multidimensional structure of a detonation wave is shown in Fig. A1. The direction of propagation of the detonation wave is to the right. The triple-point trajectory determines the boundary between each cell. For an extensive review of the cell mechanism, the reader is referred to the review paper by Lee (1984).

The width λ of an elementary cell is an important dynamic parameter of gaseous detonation. It is a direct measure of the chemical length scale of detonation, hence a measure of mixture sensitivity. For this reason, most initiation studies try to correlate cell size measurements to the energy required to directly initiate a detonation wave. The following section reports different cell size measurements for the mixtures investigated in this study.

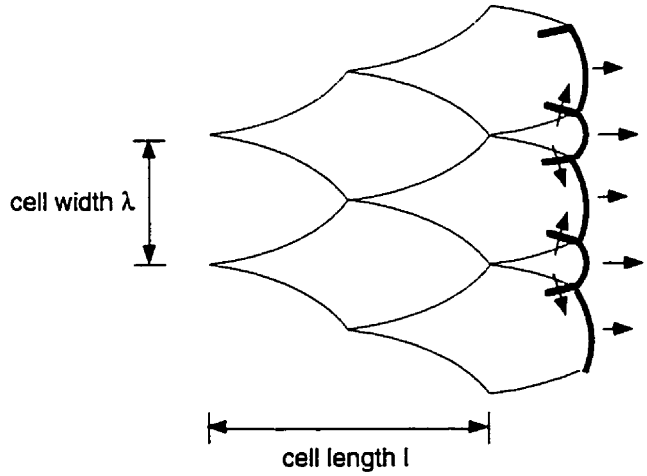

Fig. A1 Three-dimensional structure of a real detonation wave

A1.1 Acetylene-Air Mixtures

The cell size λ for a stoichiometric acetylene-air mixture is 5.8 mm, as measured by Knystautas *et al.* (1984).

A1.2 Hydrogen-Air Mixtures

The cell size λ for hydrogen-air mixtures measured by Guirao *et al.* (1982) at 1 bar initial pressure is shown in Fig. A2. It can be seen that a decrease of the fuel equivalence ratio results in larger cell sizes, hence less sensitive mixtures.

A1.3 Ethylene-Oxygen-Nitrogen Mixtures

The cell length l for various concentration of nitrogen in stoichiometric ethylene-oxygen was measured at different initial pressures by Bauer *et al.* (1986). Their measurements are shown in Fig. A3 for ratios β of nitrogen-oxygen dilution of 0.98, 3.5, 4.09, and 5. Bauer's results were curve-fit as to obtain the cell length l as a function of nitrogen dilution at 0.33 bar, 1 bar, and 3 bar. It is important to

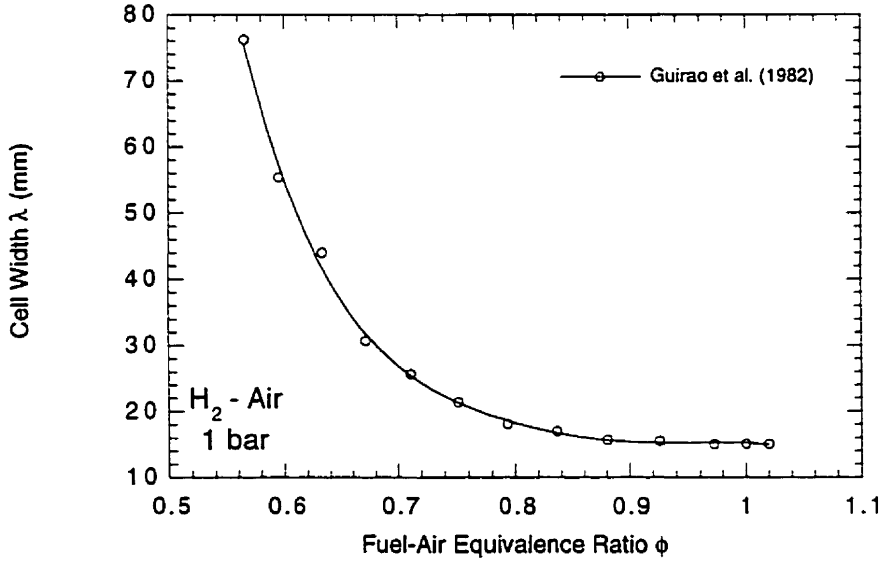

Fig. A2 Cell width measurements in hydrogen-air mixtures at 1 bar initial pressure

note that the results for 0.33 bar were extrapolated over a wide range of initial pressures, thus leading to increasing uncertainties. The cell width λ was obtained by the transformation $l = 1.6\ \lambda$, relating the length and width of a typical detonation cell. Bauer's results along with cell width measurements of other investigators (Knystautas et al. (1982,1984), Murray et al. (1984)) are plotted in Fig. A4. The λ dependence on the nitrogen dilution β can be correlated by a power law for the initial pressures of interest:

$P_o = 3$ bar $\qquad \lambda\,(\text{mm}) = 0.51195\,\beta^{2.2672}$ $\qquad$ A1

$P_o = 1$ bar $\qquad \lambda\,(\text{mm}) = 1.4553\,\beta^{2.3013}$ $\qquad$ A2

$P_o = 0.33$ bar $\qquad \lambda\,(\text{mm}) = 2.3004\,\beta^{2.728}$ $\qquad$ A3

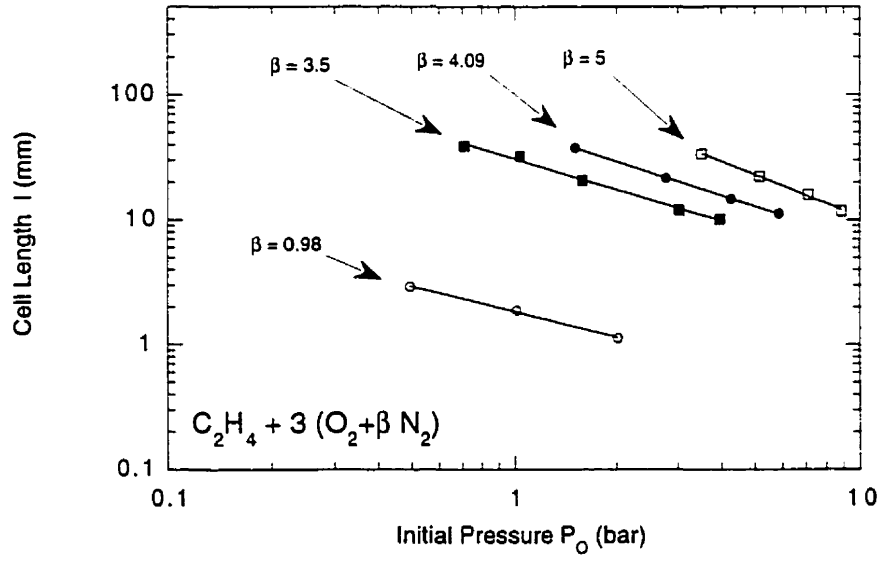

Fig. A3 Cell length measurements in stoichiometric ethylene-oxygen with variable nitrogen dilution: effect of initial pressure

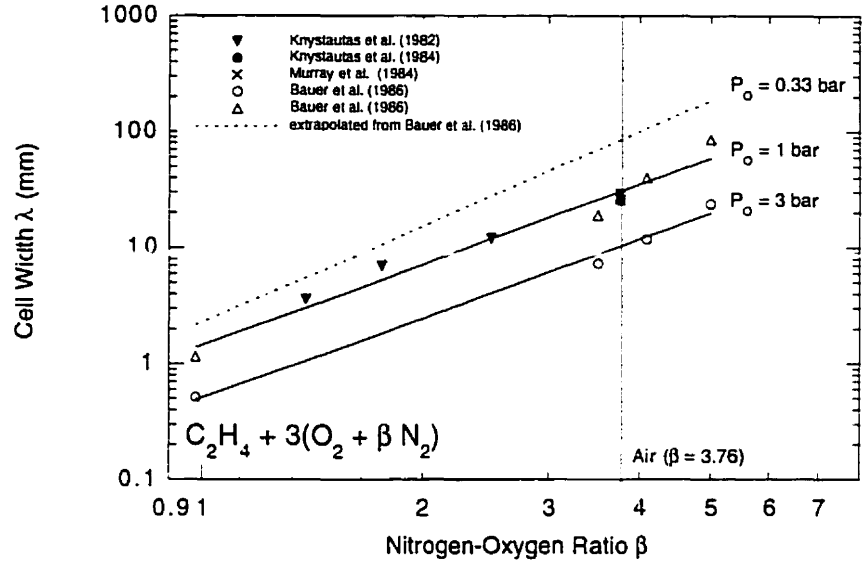

Fig. A4 Cell width of stoichiometric ethylene-oxygen with variable nitrogen dilution: effect of nitrogen dilution

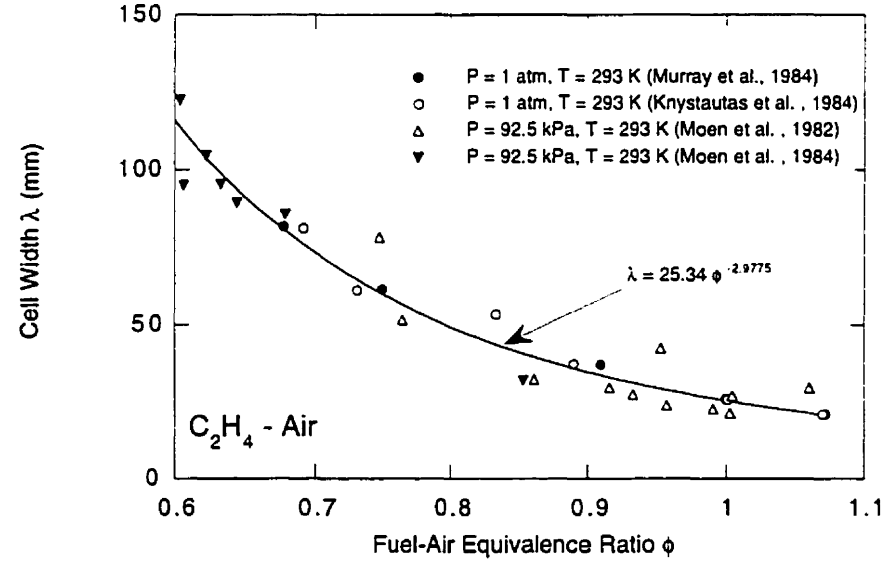

Fig. A5 Cell width measurements in ethylene-air for different stoichiometries

A1.4 Ethylene-Air Mixtures

Cell width measurements in lean ethylene-air mixtures at 0.9 - 1 bar initial pressure are plotted in Fig. A5. It can be seen that the maximum sensitivity is slightly rich mixtures. The data can be fitted accurately by a power law fit over the fuel equivalence ratio of interest (i.e. 0.6 – 1.1):

$$\lambda\,(\text{mm}) = 25.34\phi^{-2.9775} \qquad \text{A4}$$

A1.5 Methane-Oxygen Mixtures

The cell sizes of methane-oxygen mixtures, taken from the study of Aminallah *et al.* (1993), are plotted in Fig. A6 for a wide range of fuel-oxygen equivalence ratios ϕ along with the measurements of Manzhalei *et al.* (1974) and Bauer *et al.* (1985). Methane-oxygen mixtures are characterized by a very irregular cellular structure, which explains the wide scatter of the data presented in Fig. A6. A third order polynomial correlates well with the data:

$$\lambda\,(\text{mm}) = 32.051 - 67.13\phi + 47.649\phi^2 - 9.9391\phi^3 \qquad \text{A5}$$

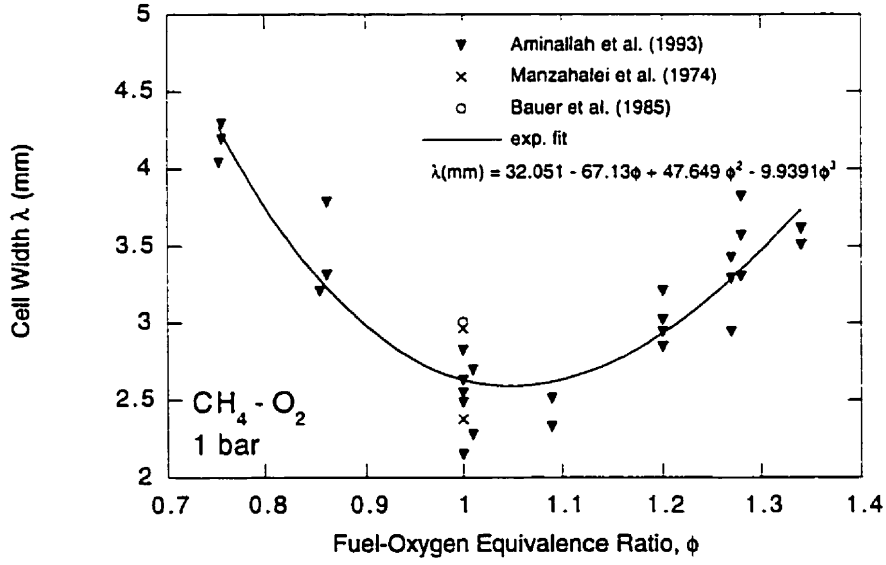

Fig. A6 Cell width measurements in methane-oxygen for different stoichiometries

A2 CJ Detonation Velocity of Mixtures Investigated

The theoretical detonation velocity V_{CJ} can be calculated from the standard Chapman-Jouguet one dimensional detonation theory. The CJ velocity and Mach number for the different mixtures investigated in this thesis were calculated with the equilibrium code STANJAN (Reynolds, 1981) using the JANNAF thermochemical data. The results are tabulated in Table A1 for acetylene-air, hydrogen-air and stoichiometric ethylene-air mixtures with variable nitrogen dilution for the critical mixtures compositions reported in Chapter 3. The CJ velocity and Mach number of ethylene-air and methane-oxygen are plotted in Figs. A7 and A8 as a function of the equivalence ratio ϕ.

Table A1 Chapman-Jouguet detonation velocities of acetylene-air, hydrogen-air and ethylene-oxygen-nitrogen mixtures

Mixture	Initial Conditions	V_{CJ}	M_{CJ}
C_2H_2 + Air $\phi = 1$	$P_O = 1$ bar $c_O = 341.6$ m/s	1867.2 m/s	5.47
H_2-Air $\phi = 0.75$	$P_O = 1$ bar $c_O = 420.5$ m/sec	2061.5 m/s	4.90
$C_2H_4 + 3(O_2 + \beta N_2)$ $\beta = 3.25$	$P_O = 1$ bar $c_O = 340.2$ m/s	1863.6 m/s	5.48
$C_2H_4 + 3(O_2 + \beta N_2)$ $\beta = 2.75$	$P_O = 0.33$ bar $c_O = 339.3$ m/s	1877.7 m/s	5.53
$C_2H_4 + 3(O_2 + \beta N_2)$ $\beta = 3.6$	$P_O = 3$ bar $c_O = 340.7$ m/s	1858.5 m/s	5.45

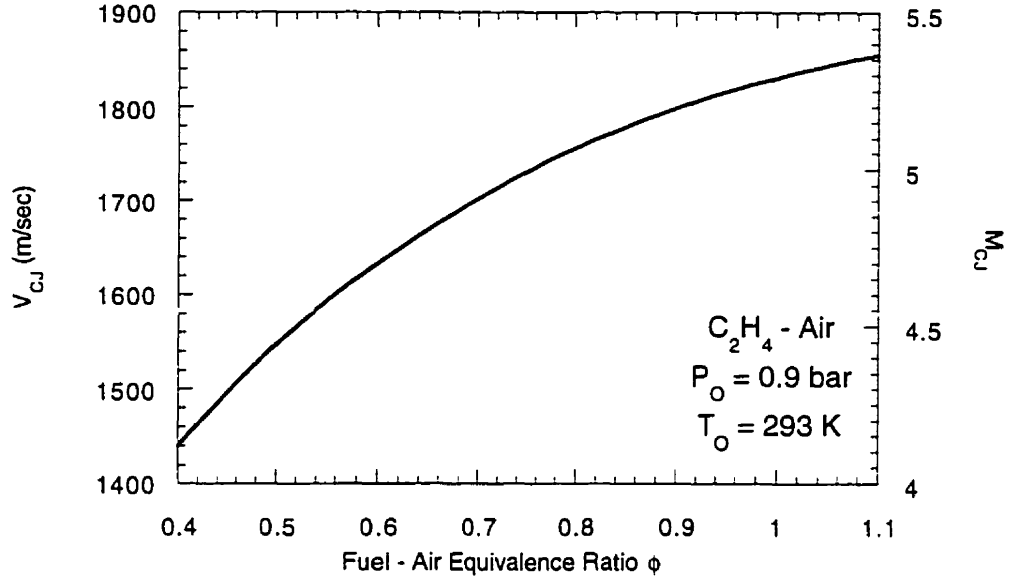

Fig. A7 Chapman-Jouguet detonation velocity and Mach number in ethylene-air

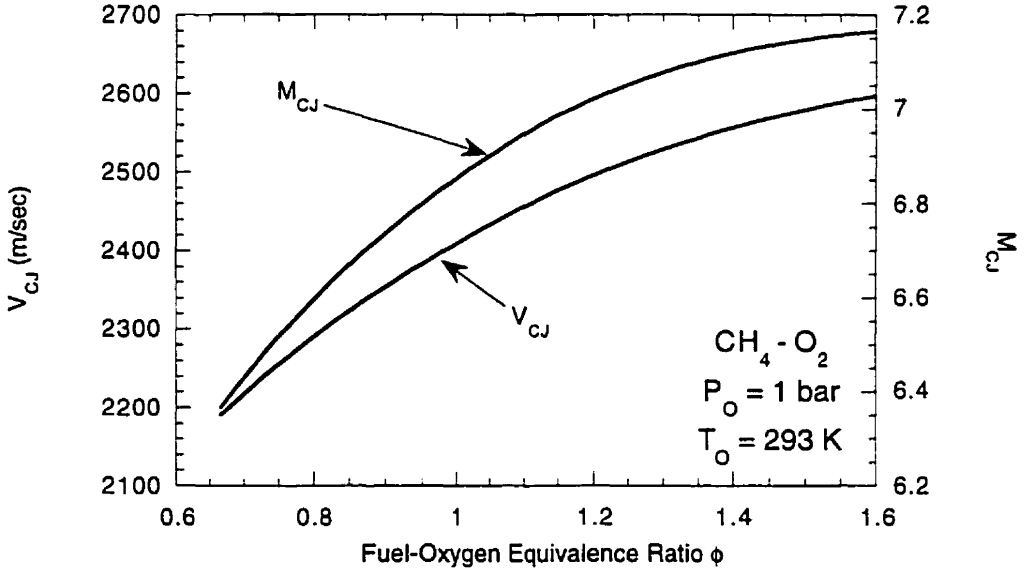

Fig. A8 Chapman-Jouguet detonation velocity and Mach number in methane-oxygen

Appendix B Raw Results for the Large-Scale Experiments

The raw results obtained in the large-scale trial series performed in C_2H_4-air are summarized below. The summary of these trials is shown in Table 1, where each shot is labeled "subcritical", "critical" or "supercritical" based on the photographic evidence of whether detonation is initiated or not.

Table B1 Summary of the different regimes observed in C_2H_4 – Air mixtures

Shot number	Percentage Fuel	Fuel-Air Equivalence Ratio ϕ	Cord Strength (kJ/m)	Comment	Regime
35	5.45	0.82	260		*supercritical*
36	6.2	0.94	260		*supercritical*
37	5	0.75	260		*subcritical*
38	5.45	0.82	520		*supercritical*
39	4.5	0.67	520		*subcritical*
40	0	0	520	shot in air	
41	6.4	0.98	260	half cord	*supercritical*
42	6.45	0.98	65		*critical*
44	6.75	1.03	65		*critical*
45	5.05	0.76	520		*supercritical*
47	4.7	0.70	520		*critical*
48	4.57	0.68	520		*critical*
49	5.35	0.81	260		*supercritical*
50	5.2	0.78	260		*supercritical*
51	6.6	1.01	91		*supercritical*
52	7	1.07	65		*supercritical*
53	7.05	1.08	65	half cord	*supercritical*

The times-of-arrival of the detonation in the cord was recorded at the ionization probes *IP1* and *IP2* (see Fig. B1). The time of arrival of the blast wave/detonation was recorded at the pressure transducers mounted on the pad floor (*PT1-PT8*). The location of these probes is shown in Fig. B1. For the first series of shots, when no ionization probes were used, the location of the detonator outside the bag and time of firing (t_0 = 5 msec) were taken as references.

The time-of-arrival of the detonation/blast wave for each trial are tabulated in Table B2. These are absolute times, 5.000 ms representing the time at which the detonator was fired. Also tabulated are the exact positions of each ionization probe along the cord with respect to the position of the detonator.

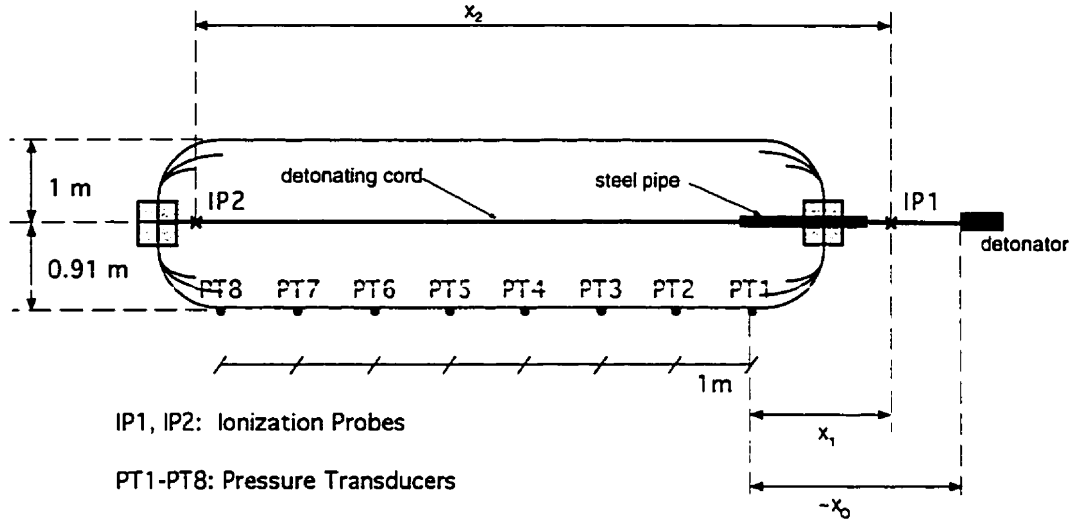

Fig. B1 Experimental diagnostics for the C_2H_4 – air large scale experiments

Table B2 Times-of-arrival of the blast/detonation at the pressure transducers and ionization probes

Shot	PT1 (ms)	PT2 (ms)	PT3 (ms)	PT4 (ms)	PT5 (ms)	PT6 (ms)	PT7 (ms)	PT8 (ms)	IP1 (ms)	IP2 (ms)	x_1 (cm)	x_2 (cm)	x_O (cm)
35	6.055	5.872					6.557						88
36	5.786	5.764	5.93	6.06	6.222	6.372	6.537	6.701					88
37		5.979	6.13	6.279	6.438	6.614	6.774	6.929					88
38		5.751	5.89	6.033	6.188	6.334	6.496	6.653					88
39		5.901	6.054	6.171	6.314	6.472		6.756					88
40			6.148	6.283	6.424	6.607	6.78	6.968					88
41	5.465	5.755	5.94	6.045	6.217	6.52	7.046	7.63					88
42		5.53	5.928	6.327	6.649	6.95	7.27	7.61					88
44		5.944	6.186	6.275	6.423	6.569	6.669	6.812	5.053	6.218	90	790	
45	6.147	5.827	5.974	6.107	6.255	6.41	6.567	6.72	5.055	6.302		820	88
47		5.873	6.031	6.203	6.297	6.443	6.713	6.799		6.28	90	800	88
48		5.929	6.053	6.2	6.362	6.472	6.661	6.837	5.029	6.265	93	800	
49		5.855	6.001	6.148	6.299	6.463	6.636	6.794	5.058	6.287	82	770	
50		5.836	5.98	6.138		6.447	6.614	6.814	5.019	6.366	90.5	830	
51		5.808	5.94	6.078	6.218	6.354	6.511	6.655	5.032	6.175	77.5	800	
52		5.821	5.961	6.101	6.252	6.418	6.566		5.03	6.255	88.5	800	

In Table B3 are tabulated the detonation velocity in the cord, as measured from the time of arrival of the detonation at ionization probes IP1 and IP2. The error in the VOD measurements is estimated at approximately 5%. Within the

experimental error, this velocity is constant for each size of detonating cord. The discrepancies in velocities between the different types of cords can be attributed to the different packing densities in the PETN content of the cord.

Table B3 Measures of detonating cord velocity

Shot	44	45	48	49	50	51	52
Cord Strength (kJ/m)	65	520	520	260	260	91	65
VOD (km/sec)	6.78	6.58	6.47	6.27	6.16	7.00	6.53

The velocity of the blast wave/detonation between the pressure transducers located on the pad floor are tabulated in Table B4 for the mid-point between two successive transducers. In Table B5 are tabulated the velocities of the blast wave/detonation between the detonating cord and the pressure transducers on the pad floor.

Table B4 Blast wave velocity measured from the pressure transducers TOA's along the pad floor (in km/sec)

Shot x(m)	1.5	2.5	3.5	4	4.5	5.5	6	6.5	Average
35			7.30						**7.29**
36	6.02	7.69	6.17		6.66	6.06		6.09	**6.45**
37	6.62	6.71	6.28		5.68	6.25		6.45	**6.33**
38	7.19	6.99	6.45		6.84	6.17		6.36	**6.67**
39	6.53	8.54	6.99		6.39		7.04		**7.08**
40		7.40	7.09		5.46	5.78		5.31	**6.21**
41	5.40	9.52	5.81		3.30	1.90		1.71	**4.60**
42	2.51	2.50	3.10		3.32	3.12		2.94	**2.91**
44	4.13	11.23	6.75		6.84	10.00		6.99	**7.66**
45	6.80	7.51	6.75		6.45	6.36		6.53	**6.73**
47	6.32	5.81	10.63		6.84	3.70		11.62	**7.49**
48	8.06	6.80	6.17		9.09	5.29		5.68	**6.85**
49	6.84	6.80	6.62		6.09	5.78		6.32	**6.41**
50	6.94	6.32		6.47		5.98		5.00	**6.14**
51	7.57	7.24	7.14		7.35	6.36		6.94	**7.10**
52	7.14	7.14	6.62		6.02	6.75			**6.73**

Table B5 Velocity measurements between the detonating cord and the pressure transducers on the pad floor

Shot	Cord-PT2 km/sec	Cord-PT3 km/sec	Cord-PT4 km/sec	Cord-PT5 km/sec	Cord-PT6 km/sec	Cord-PT7 km/sec	Cord-PT8 km/sec	Average km/sec
35	1.60					2.02		**1.81**
36	1.97	1.95	2.09	2.08	2.14	2.12	2.10	**2.06**
37	1.35	1.37	1.39	1.39	1.36	1.36	1.38	**1.37**
38	1.97	2.03	2.08	2.07	2.10	2.06	2.04	**2.05**
39	1.48	1.49	1.58	1.61	1.59		1.66	**1.57**
40		1.29	1.32	1.35	1.29	1.25	1.20	**1.28**
41	2.01	1.91	2.16	2.11	1.59	0.97	0.67	**1.63**
42		1.84	1.22	0.99	0.85	0.74	0.64	**1.05**
44	1.50	1.31	1.43	1.44	1.45	1.57	1.59	**1.47**
45	1.69	1.71	1.78	1.79	1.79	1.78	1.78	**1.76**
47	1.56	1.54	1.50	1.66	1.68	1.38	1.54	**1.55**
48	1.51	1.58	1.60	1.58	1.70	1.60	1.54	**1.59**
49	1.81	1.86	1.91	1.96	1.94	1.89	1.91	**1.90**
50	1.78	1.84	1.86		1.91	1.88	1.74	**1.83**
51	1.74	1.78	1.80	1.81	1.83	1.78	1.78	**1.79**
52	1.79	1.83	1.87	1.86	1.81	1.81		**1.83**